A consistent phase-field-regularised partition of unity method for fracture analysis

Farshid Fathi*, René de Borst, Giacomo Torelli

School of Mechanical, Aerospace and Civil Engineering, University of Sheffield, Sir Frederick Mappin Building (Broad Lane Building), Mappin Street, Sheffield, S1 3JD, UK

Abstract

Recent advancements in phase-field models have significantly reshaped the landscape of fracture mechanics, which was dominated by the partition of unity method in the early 21st century. In this study, we aim to leverage the advantages of the two approaches by adopting a novel phase-field-regularised partition of unity method to improve computational efficiency, robustness and physical consistency. Specifically, we establish a connection between early phase-field models and the partition of unity method for cohesive fracture. To this end, we replace the standard discontinuous Heaviside enrichment in the partition of unity method with a regularised and continuous Heaviside function, leveraging the phase-field approximation of the Dirac-δ function. The proposed formulation effectively resolves ill-conditioning issues in the traditional partition of unity method while retaining the key advantages of discrete fracture representations, offering a distinct contrast to traditional phase-field approaches for smeared crack models. These advantages include eliminating the need for extremely fine meshes and providing an unambiguous and physically consistent representation of the displacement jump across a crack. Furthermore, by integrating Non-Uniform Rational B-Splines (NURBS) for spatial discretisation, the approach enhances solution accuracy compared to standard finite element formulations. Compatibility enforcement is also modified to accommodate the crack diffused by the phase-field approximation. Through numerical examples, including stationary and propagating cracks, mesh refinement studies, and sensitivity analyses of the

* *Email address:* `f.fathi@sheffield.ac.uk` (Farshid Fathi)

phase-field length scale, we establish an optimal prescription for the internal length scale based solely on the element size. The examples compare the results obtained via the presented formulations with exact solutions and other numerical techniques, demonstrating the accuracy, conditioning stability, and computational efficiency of the methodology. The proposed methodology thus presents a robust alternative to conventional fracture models, combining key advantages offered by discrete and smeared approaches.

Keywords: Phase-field model, extended finite element analysis, isogeometric analysis, partition of unity method

1. Introduction

Fracture mechanics has always been an important topic of study in engineering, and has attracted various numerical approaches to simulate the fracture process effectively. At the early stages, the theorem of minimum energy was developed for a predefined crack in an elastic solid [1] inspired by the observation of unbounded (singular) stresses in the vicinity of a sharp notch [2], rendering the stresses useless for determination of crack propagation. Griffith's theory of brittle fracture was expanded to ductile materials [3], and later generalised for elastic-plastic solids [4]. A common feature of all the previously mentioned contributions is the relatively small fracture process zone compared to the size of the structure, which limits the focus to Linear Elastic Fracture Mechanics (LEFM). Additionally, they fail to model crack nucleation in an undamaged area away from the discontinuity and to predict the direction of the crack growth except through *a posteriori* studies [5], which required remeshing at the crack front after propagation. New techniques were developed to address these issues in numerical fracture modelling, following two main trends: smeared approaches, which account for deterioration of the stiffness of the material in the micro-structure; and discrete models, which explicitly represent fractures as distinct geometrical entities, generating a discontinuous displacement field.

The smeared approaches involve embedding strain localisation within an element [6, 7], for instance, through the presence of high deformation gradients due to fracture. The displacement discontinuity is represented through an additional, incompatible, Dirac-δ strain term [8], where the so-called embedded crack is diffused within the element. Different variants of the embedded discontinuity approach have been put forth [9], and comparative studies

have been conducted [10]. One of the main issues which adhere to the embedded approach is the ill-posedness in the presence of strain softening, which necessitates using extra information, such as incorporating higher-order derivatives of displacement in the kinematics [11, 12] or adding non-local terms [13], which are typically referred to as regularisation models. However, the proposed remedies often do not yield a symmetric stiffness matrix, and retrieving the crack opening displacement is non-trivial [14, 15].

In the context of discrete fracture models, a displacement discontinuity can be incorporated into continuum mechanics through a rigorous definition of the fracture by extra degrees of freedom (DOFs). This can be obtained either through interface elements located in between standard continuum elements [16, 17], or via Partition of Unity Method (PUM) [18], which allows for local enrichment of nodal points of the cracked element with extra DOFs, known as extended finite element analysis [19]. In this manuscript, we distinguish eXtended Finite Element Method (XFEM), where Lagrange polynomials are utilised as shape functions, from the broader term extended finite element analysis, referring to a larger family of enriched approaches including eXtended IsoGeometric Analysis (XIGA) [20]. The enriched approach decouples the crack path and the mesh layout, allowing both inter- and intra-element fractures which enable arbitrary crack propagation. This flexibility is absent in interface elements as the crack extension path should be known *a priori*. Moreover, since interface elements are inserted in advance, a dummy stiffness must be adopted to avoid premature crack growth, which can lead to spurious stress oscillations if the dummy stiffness is too high [17]. The cohesive zone model, an extension of LEFM in the presence of non-negligible fracture process zone [21, 22], is widely used in discrete models, including interface elements [23] and XFEM [24].

More recently, efforts have been primarily devoted to phase-field models to simulate the fracture process. These models trace back to the minimisation of the total energy based on Griffith's theory of brittle fracture [25] and its regularised form [26]. Afterwards, a majority of the phase-field literature has been devoted to brittle fracture [27, 28, 29, 30, 31, 32, 33] and, by way of analogy to gradient-enhanced damage mechanics [34, 35], expanded to ductile fracture [36, 37, 38]. Regarding the cohesive-zone phase-field models, two alternative approaches can be identified: (i) the traction-separation relationship is applied to a crack diffused by the phase-field approximation of the Dirac-δ, without any explicit degradation function used for the deterioration of the bulk material [32, 39, 40, 41, 42]; (ii) a tailored degradation function,

characterised and tuned through a uniform tension test, is applied to the bulk material to replicate the mechanical response of a certain traction-separation relationship [43, 44], analogous to gradient damage models [45]. In this work, we aim at enhancing the former through Partition of Unity Method (PUM), while involving a degradation function will be explored in a future work. It will be shown in the remainder that the former is reminiscent of regularised discrete fracture models, for instance the regularised XFEM [46].

Extended finite element analysis requires crack tracking strategies, such as level-set [47, 48] and fast marching [49, 50] methods, to define the tangential and normal vectors on the crack profile needed for the Heaviside function. However, crack branching or coalescence pose significant challenges, such as non-unique normal vectors at crack intersections, which becomes even more difficult when accounting for three-dimensional problems [51]. In contrast, phase-field models eliminate the need for crack tracking through adding a separate differential equation for the crack profile, allowing for simulating crack propagation, coalescence and branching, particularly in three-dimensional cases. However, this comes at the expense of utilising a very fine mesh [40]. To leverage the advantages of XFEM and phase-field models, several hybrid approaches have been developed. For instance, in the context of LEFM, a multi-resolution global-local enrichment is utilised for extended/generalised finite element method. The phase-field model is only used for crack advancement at the fine scale in the vicinity of the crack tip, while XFEM handles the discontinuity elsewhere [52]. Another approach involves using XFEM for the large scale displacement field, while a local phase-field solution determines the crack propagation at the crack tip(s) for LEFM [53]. Taking advantage of the known exponential form of a typical phase-field solution, exponential shape functions were proposed to reduce the number of elements perpendicular to the crack path, while a fine mesh is still needed in the parallel direction [54]. The ansatz presented in [54] for phase-field was recently transformed to resolve compatibility issues and combined with XFEM for brittle fracture [55]. Additionally, Thick Level-Set (TLS) method, a level-set-based damage model [56], was successfully compared with phase-field models for brittle and quasi-brittle fracture [57].

A well-known issue in extended finite element analysis is the ill-conditioning of the stiffness matrix in certain scenarios, which can lead to the loss of accuracy or, in case of linear dependency, results in a singular stiffness matrix [58]. This typically occurs when the crack (i) aligns very close to the element edge or (ii) divides the element into highly disproportionate sections,

making it impossible to place sufficient integration points on one side of the crack to properly account for the Heaviside enrichment [58, 59]. The mesh-independent nature of extended finite element analysis generally makes it difficult to avoid these scenarios, particularly in arbitrary propagating crack problem. Several approaches have been proposed to mitigate the conditioning issue, such as perturbation of the stiffness matrix [60, 61] or preconditioning based on domain decomposition [62]. Retrieving the convergence rate of finite element analysis is the objective of a few other contributions [58, 63, 64]. All of these attempts, however, fail to directly resolve the robustness issue associated with the Heaviside enrichment in the ill-conditioning scenarios [65]. Instead, *a posteriori* re-arrangement of the mesh layout is the typical indirect solution to both scenarios. Node snapping is an example, where nodes are moved away from the crack path to resolve the conditioning issue.[59] However, this approach nullifies the computational advantages given by decoupling the crack path from the mesh layout in XFEM. Another remedy involves deviating the crack path [66, 67], even though extra care must be taken to limit the deviation to avoid other conditioning issues [59]. An alternative to avoid the linear dependency is orthonormalisation of shape functions, as applied in XFEM [68] and in XIGA [69], however this approach does not solve ill conditioning issues associated with cracks that split an element disproportionately.

On the other hand, IsoGeometric Analysis (IGA) tends to outperform the standard Finite Element Analysis (FEA) in accurate representation of the geometry [70], versatility in providing arbitrary degree of (higher-order) continuity at element boundaries [71], and a per-degree-of-freedom superiority in accuracy and robustness [72, 73]. Non-Uniform Rational B-splines (NURBS) are adopted in the present work. Regarding fracture, IGA was first cast in an extended finite element analysis format, coined XIGA, for LEFM [20], and later expanded to cohesive fracture [74]. IGA has been incorporated in cohesive interface elements approach for fracture simulation as well [75]. Recently, blending XIGA with a meshfree method has successfully mitigated the conditioning issue of the stiffness matrix associated with the Heaviside function [76], as no fixed notion of spatial discretisation exist. Instead, the overlapping support clouds of points provide sufficient space for the Heaviside function integration in extreme scenarios of disproportionate fracture.

Herein, we aim at regularising XIGA using phase-field approximation of the Dirac-δ, enabled through the use of continuous exponential decay function to regularise the Heaviside and the signed-distance level set functions by

taking into account the relationship between these quantities. The concept of regularised Heaviside function has already been implemented for XFEM [46, 77, 78], but these formulations fail to enforce compatibility constraints and provide suitable guidelines for defining an appropriate regularization length scale, all of which are further complicated in the context of IGA. For instance, the inter-element sharing of control points complicates enrichment, rendering the use of the standard enrichment prescription for the regularised formulation questionable. In addition, it is imperative to investigate whether the regularised formulation mitigates the conditioning issue of the stiffness matrix associated with the Heaviside enrichment.

This work addresses the above-mentioned challenges by developing a formulation that regularises XIGA using a phase-field approximation of the Dirac-δ, enforces compatibility for diffused crack descriptions, accommodates nonlinear traction-separation relationships, and defines a spatially varying length scale based on the characteristic element size. The article is structured as follows. Section 2 presents the ingredients at the bulk and the discontinuity for a phase-field regularised PUM for fracture analysis, followed by the variational forms of the displacement and the phase-field in Section 3. Next, the discretisation of the weak forms are discussed in Section 4, along with a succinct introduction of NURBS formulated on Bézier-extraction to comply with finite element data-structure [79]. Section 5 discusses implementation aspects, including compatibility enforcement of the regularised formulation, the enrichment scheme and the integration strategy utilised. Finally, some case studies, comprised of mesh refinement and singularity analysis for traction-free cracks and cohesive fractures, are examined to demonstrate the efficacy of the proposed formulation. Stationary and progressive fracturing are explored in Section 6, while rate-independent materials are assumed and isotropic elasticity is utilised for the bulk and the regularised layer.

2. Phase-field regularised partition of unity method

The partition of Unity Method (PUM) has been proven effective in approximating non-uniform fields with local high gradients. This is, for instance, the case when dealing with fractures, as a discontinuity Γ_{d} is shown within a continuous body Ω in Figure 1. PUM [60] approximates the additional field by means of an enrichment function γ and the set of shape functions $\boldsymbol{\varphi}$,

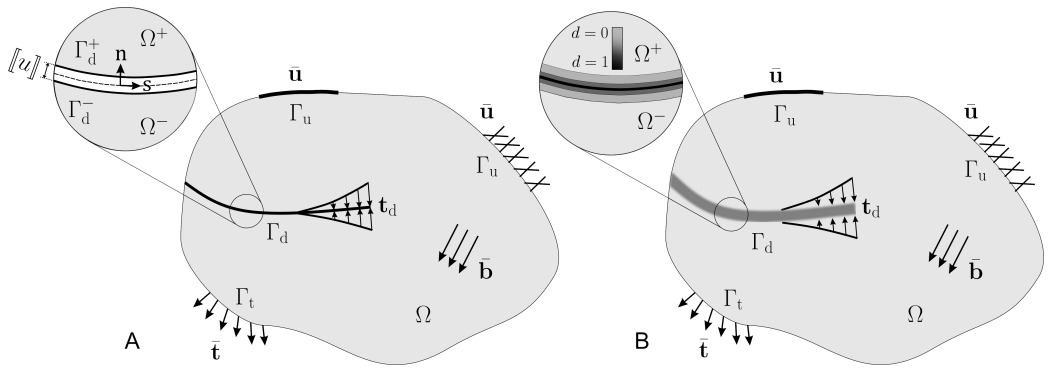

Figure 1: Boundary value problem Ω with the discontinuity Γ_d and cohesive tractions $\mathbf{t}_d$: A) a sharp crack B) a diffused description of the discontinuity.

$$a^{\mathrm{h}}_{\mathrm{PUM}} = \sum_i \varphi_i(x) \left(\sum_j a_{ij} \gamma_j(x) \right) \quad \text{where} \quad \sum_i \varphi_i(\mathbf{x}) = 1 \quad \forall \mathbf{x} \in \Omega \tag{1}$$

where $\bullet^{\mathrm{h}}$ denote the approximated $\bullet$ field. Enriching the Finite Element Analysis (FEA) with PUM leads to Generalised Finite Element Method (GFEM) [60, 80] in terms of standard and (extrinsically[81]) enriched discrete nodal values, $\hat{\bullet}$ and $\tilde{\bullet}$, respectively

$$a^{\mathrm{h}} = \sum_i \hat{\varphi}_i(x)\, \hat{a}_i + \sum_i \tilde{\varphi}_i(x) \left(\sum_j \tilde{a}_{ij} \mathscr{H}_j(x) \right). \tag{2}$$

Using the Heaviside sign function, GFEM is capable of representing a fractured body similar to Figure 1 through

$$\mathbf{u}^{\mathrm{h}} = \hat{\mathbf{u}}^{\mathrm{h}} + \mathscr{H}_{\Gamma_{\mathrm{d}}}\, \tilde{\mathbf{u}}^{\mathrm{h}} \quad \text{with} \quad \mathscr{H}_{\Gamma_{\mathrm{d}}}(x_{\mathrm{n}}) = \{1 \,|\, \forall x_{\mathrm{n}} > 0; -1 \,|\, \forall x_{\mathrm{n}} < 0; 0 \,|\, x_{\mathrm{n}} = 0\}, \tag{3}$$

where $\mathbf{u}$, $\hat{\mathbf{u}}$ and $\tilde{\mathbf{u}}$ indicate the total, continuous and discontinuous displacement fields, respectively. Dealing with cracks and voids, GFEM is referred to as extended finite element analysis, and has been widely used for different applications using Lagrange polynomials [81, 82, 83], or by means of spline technologies for isogeometric analysis [73, 76, 84].

In the absence of the acceleration, the quasi-static equilibrium equations read

$$
\begin{cases}
-\nabla \cdot \boldsymbol{\sigma} = & \bar{\mathbf{b}} & \mathbf{x} \in \Omega \\
\mathbf{u}^{\mathrm{h}} = & \bar{\mathbf{u}} & \mathbf{x} \in \Gamma_{\mathrm{u}} \\
\boldsymbol{\sigma} \cdot \mathbf{n}_{\mathrm{t}} = & \bar{\mathbf{t}} & \mathbf{x} \in \Gamma_{\mathrm{t}} \\
\boldsymbol{\sigma} \cdot \mathbf{n}_{\mathrm{d}} = & \mathbf{t}_{\mathrm{d}} & \mathbf{x} \in \Gamma_{\mathrm{d}}
\end{cases}
\tag{4}
$$

where $\boldsymbol{\sigma}$ is the Cauchy stress tensor, $\mathbf{n}_{\mathrm{d}}$ and $\mathbf{n}_{\mathrm{t}}$ are the vectors normal to the fracture surface Γ_{d} and the external traction surface Γ_{t}, respectively. The prescribed values for displacements, tractions and body forces are referred to as $\bar{\mathbf{u}}$, $\bar{\mathbf{t}}$ and $\bar{\mathbf{b}}$, respectively. We apply the weighted residual method to the strong form in Equation (4) and utilise the divergence theorem to define a general weak form of the potential energy as

$$
\Psi_{\mathrm{pot}} = \overbrace{\int_{\Omega} \psi \left(\boldsymbol{\varepsilon}(\mathbf{u}^{\mathrm{h}})\right) \, \mathrm{d}\Omega}^{\mathcal{E}_{\mathrm{int}}} - \overbrace{\left(\int_{\Gamma_{\mathrm{t}}} \bar{\mathbf{t}} \cdot \mathbf{u}^{\mathrm{h}} \, \mathrm{d}\Gamma + \int_{\Omega} \bar{\mathbf{b}} \cdot \mathbf{u}^{\mathrm{h}} \, \mathrm{d}\Omega \right)}^{\mathcal{P}_{\mathrm{ext}}}
\tag{5}
$$

where $\mathcal{E}_{\mathrm{int}}$ and $\mathcal{P}_{\mathrm{ext}}$ indicate internal and external energy functions. The strain energy function ψ reads,

$$
\psi = \frac{1}{2} \boldsymbol{\sigma} : \boldsymbol{\varepsilon}.
\tag{6}
$$

Unlike explicit description of fracture by Griffith's potential energy function [39, 25, 26], which allocates a distinct energy term to the fracture, we aim to construct the fracture energy term from the displacement discontinuity, which is characterised by the Heaviside function $\mathscr{H}_{\Gamma_{\mathrm{d}}} = \mathbf{n}_{\mathrm{d}} \cdot \boldsymbol{\nabla} \mathscr{D}_{\Gamma_{\mathrm{d}}}$. Here, $\mathscr{D}_{\Gamma_{\mathrm{d}}}$ denotes the sign distance function, as illustrated in Figure 2.

Adopting the small displacement assumption, the infinitesimal strain field becomes

$$
\boldsymbol{\varepsilon} = \boldsymbol{\nabla}^{\mathrm{s}} \mathbf{u}^{\mathrm{h}} = \underbrace{\boldsymbol{\nabla}^{\mathrm{s}} \hat{\mathbf{u}}^{\mathrm{h}}}_{\text{continuous}} + \underbrace{\mathscr{H}_{\Gamma_{\mathrm{d}}} \boldsymbol{\nabla}^{\mathrm{s}} \tilde{\mathbf{u}}^{\mathrm{h}} + 2\delta_{\Gamma_{\mathrm{d}}} \left(\tilde{\mathbf{u}}^{\mathrm{h}} \otimes^{\mathrm{s}} \mathbf{n}_{\mathrm{d}} \right)}_{\text{discontinuous}}
\tag{7}
$$

where $\boldsymbol{\nabla}^{\mathrm{s}} \square = (\boldsymbol{\nabla} \square + \boldsymbol{\nabla} \square^{\mathrm{T}})/2$, $\otimes^{\mathrm{s}}$ indicates the symmetric tensor product, and $\delta_{\Gamma_{\mathrm{d}}}$ is the Dirac-delta at Γ_{d}, *i.e.*, $\delta_{\Gamma_{\mathrm{d}}} = \delta_{\mathrm{Dirac}} (\mathbf{x} - \mathbf{x}_{\mathrm{c}})$ with $\mathbf{x}_{\mathrm{c}} = \operatorname{argmin} (\|\mathbf{x}^* - \mathbf{x}\|) \; \forall \mathbf{x}^* \in \Gamma_{\mathrm{d}}$ [39], which follows the identity $\mathbf{n}_{\mathrm{d}} \cdot \boldsymbol{\nabla} \mathscr{H}_{\Gamma_{\mathrm{d}}} = 2\delta_{\Gamma_{\mathrm{d}}}$.

Equation 7 can be expressed for strain components at the bulk and the discontinuity, *i.e.*, $\boldsymbol{\varepsilon} = \boldsymbol{\varepsilon}^{\mathrm{b}} + \boldsymbol{\varepsilon}^{\Gamma_{\mathrm{d}}}$

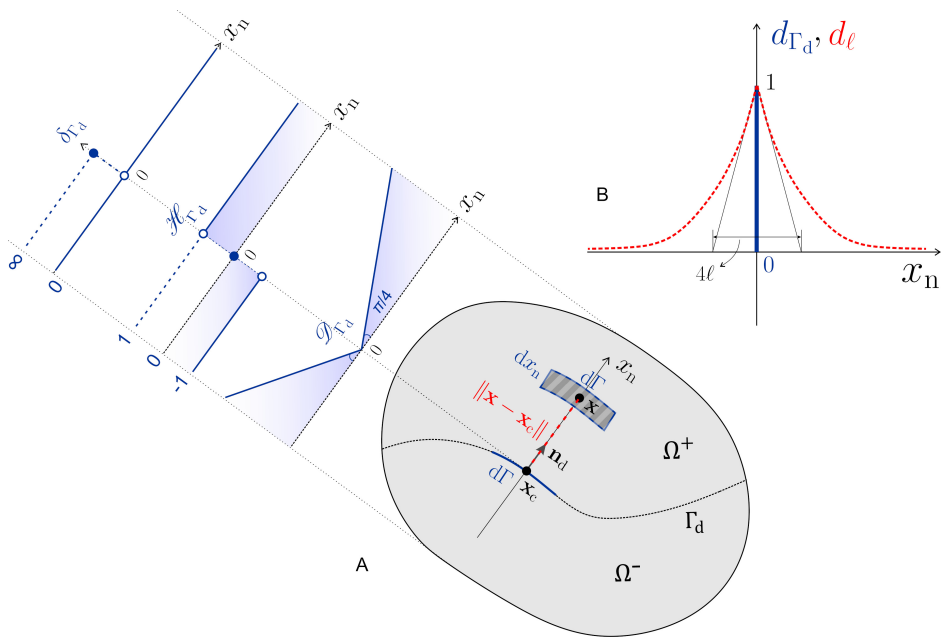

Figure 2: Consistent definition of the discontinuity: A) signed distance function $\mathscr{D}_{\Gamma_d}$, Heaviside sign function $\mathscr{H}_{\Gamma_d}$ and Dirac-delta function δ_{Γ_d}, B) Sharp and diffused definition of the phase-field variable, d_{Γ_d} and d_ℓ respectively.

$$\boldsymbol{\varepsilon}^{\mathrm{b}} = \boldsymbol{\nabla}^{\mathrm{s}}\hat{\mathbf{u}}^{\mathrm{h}} + \mathscr{H}_{\Gamma_d}\,\boldsymbol{\nabla}^{\mathrm{s}}\tilde{\mathbf{u}}^{\mathrm{h}} \qquad \text{and} \qquad \boldsymbol{\varepsilon}^{\Gamma_d} = 2\delta_{\Gamma_d}\left(\tilde{\mathbf{u}}^{\mathrm{h}} \otimes^{\mathrm{s}} \mathbf{n}_{\mathrm{d}}\right). \tag{8}$$

Inserting Equation (8) into (5) and utilising the identity $(\square \otimes^{\mathrm{s}} \bullet) : \bigcirc = \bigcirc \cdot \bullet \cdot \square$ leads to the internal potential energy of the form

$$\mathcal{E}_{\mathrm{int}} = \int_\Omega \psi^{\mathrm{b}}\left(\boldsymbol{\varepsilon}^{\mathrm{b}}(\mathbf{u}^{\mathrm{h}})\right)\,\mathrm{d}\Omega + \int_\Omega \delta_{\Gamma_d}\,\mathbf{t}_{\mathrm{d}} \cdot \tilde{\mathbf{u}}^{\mathrm{h}}\,\mathrm{d}\Omega \tag{9}$$

where $\mathbf{t}_{\mathrm{d}} = \boldsymbol{\sigma} \cdot \mathbf{n}_{\mathrm{d}}$ indicates the traction vector at the discontinuity and

$$\psi^{\mathrm{b}} = \frac{1}{2}\boldsymbol{\sigma} : \boldsymbol{\varepsilon}^{\mathrm{b}} \quad \text{with} \quad \boldsymbol{\sigma} = \mathbb{C}\,\boldsymbol{\varepsilon}^{\mathrm{b}} \tag{10}$$

following the Hooke's law for an isotropic linear elastic material where $\mathbb{C}$ indicates the stress-strain relationship.

The key difference between the discrete and regularised approaches emerges in Equation (9), depending on how the last term is interpreted,

$$\overbrace{\int_{\Gamma} \phi(\mathbf{x})\,\mathrm{d}\Gamma}^{\text{discrete}} \longleftarrow \int_{\Omega} \delta_{\Gamma_\mathrm{d}}(\mathbf{x})\,\phi(\mathbf{x})\,\mathrm{d}\Omega \longrightarrow \overbrace{\int_{\Omega} \delta_{\ell}\phi(\mathbf{x})\,\mathrm{d}\Omega}^{\text{smeared}} \tag{11}$$

where $\phi(\mathbf{x})$ is an arbitrary continuous function, and δ_ℓ represents the diffused estimate of the Dirac-δ function with the internal length scale parameter $\ell \in \mathbb{R}^+$. Fracture energy, the energy dissipated upon creation of a unit fracture surface, reads

$$\mathcal{G}_\mathrm{f} = \mathbf{t}_\mathrm{d} \cdot \tilde{\mathbf{u}}^\mathrm{h} = \frac{1}{2}\mathbf{t}_\mathrm{d} \cdot [\![\mathbf{u}]\!] \tag{12}$$

where

$$[\![\mathbf{u}]\!] = \left(\mathbf{u}^\mathrm{h}\right)^+ - \left(\mathbf{u}^\mathrm{h}\right)^- = \left(\mathscr{H}^+_{\Gamma_\mathrm{d}} - \mathscr{H}^-_{\Gamma_\mathrm{d}}\right)\tilde{\mathbf{u}}^\mathrm{h} = 2\tilde{\mathbf{u}}^\mathrm{h} \tag{13}$$

denotes the displacement jump, derived by taking advantage of the explicit definition of the discontinuity in the discrete approach through the Heaviside sign function, see Equation (3).

Utilising these findings, Equation (5) becomes

$$\Psi_\mathrm{pot} = \int_\Omega \psi^\mathrm{b}\left(\boldsymbol{\varepsilon}^\mathrm{b}(\mathbf{u}^\mathrm{h})\right)\,\mathrm{d}\Omega + \int_\Omega \delta_{\Gamma_\mathrm{d}}\,\mathcal{G}_\mathrm{f}\,\mathrm{d}\Omega - \int_{\Gamma_\mathrm{t}} \bar{\mathbf{t}} \cdot \mathbf{u}^\mathrm{h}\,\mathrm{d}\Gamma - \int_\Omega \bar{\mathbf{b}} \cdot \mathbf{u}^\mathrm{h}\,\mathrm{d}\Omega \tag{14}$$

which is identical to the Griffith potential energy used in other cohesive phase-field models [25, 32, 39, 41, 43, 52].

2.1. Dirac-delta approximation

Now, we provide a smeared approximate of $\delta_{\Gamma_\mathrm{d}}$ by means of an exponential decay [29, 30, 39]

$$\delta_{\Gamma_d}(x_\mathrm{n}) \approx \delta_\ell(x_\mathrm{n}) = \frac{1}{2\ell}\exp\left(-\frac{|x_\mathrm{n}|}{\ell}\right), \tag{15}$$

where $x_\mathrm{n} = (\mathbf{x} - \mathbf{x}_\mathrm{c}) \cdot \mathbf{n}_\mathrm{d}(\mathbf{x}_\mathrm{c})$, and $\mathbf{n}_\mathrm{d}(\mathbf{x}_\mathrm{c})$ is the unit vector normal to the interface at $\mathbf{x}_\mathrm{c}$, which is in-line with the signed distance function $\mathscr{D}_{\Gamma_\mathrm{d}} = |(\mathbf{x}-\mathbf{x}_\mathrm{c})\cdot\mathbf{n}_\mathrm{d}| = ||\mathbf{x}-\mathbf{x}_\mathrm{c}||\,\mathrm{sign}\left((\mathbf{x}-\mathbf{x}_\mathrm{c})\cdot\mathbf{n}_\mathrm{d}\right)$, see Figure 2, with the Euclidean norm shown by $||\square||$.

In order to avoid the ambiguities associated with generalisation of Equation (15) to multi dimensions [35, 39], the phase-field variable, $d \in [0,1]$, was proposed which describes the state of the material: $d = 0$ for intact and $d = 1$ for fully broken materials. The phase-field variable $d = \exp\left(-\frac{|x_\mathrm{n}|}{2\ell}\right)$ is the solution of the Euler-Lagrange equation subjected to the constraints

$$\begin{cases} d - 4\ell^2 \boldsymbol{\nabla}^2 d = \ \ 0 & \mathbf{x} \in \Omega \backslash \Gamma_\mathrm{d} \\ d = 1 & \mathbf{x} \in \Gamma_\mathrm{d} \\ \boldsymbol{\nabla} d \cdot \mathbf{n}_{\partial\Omega} = 0 & \mathbf{x} \in \partial\Omega = \{\Gamma_\mathrm{t}, \Gamma_\mathrm{u}\} \end{cases} . \tag{16}$$

that is associated with

$$d^\mathrm{h} = \arg\left\{\inf_{d^\mathrm{h} \in \mathcal{S}_d} \int_\Omega \delta_\ell(d^\mathrm{h})\, \mathrm{d}\Omega\right\}, \tag{17}$$

where d^h denotes the approximated phase-field variable, the phase-field space $\mathcal{S}_d = \left\{d^\mathrm{h} | d^\mathrm{h}(\mathbf{x}) = 1 \ \ \forall \mathbf{x} \in \Gamma_\mathrm{d}\right\}$ and

$$\delta_\ell = \frac{1}{4\ell}\left(d^\mathrm{h} \cdot d^\mathrm{h} + 4\ell^2 \frac{\partial d^\mathrm{h}}{\partial x_\mathrm{n}} \cdot \frac{\partial d^\mathrm{h}}{\partial x_\mathrm{n}}\right) = \frac{1}{4\ell}\left(d^\mathrm{h} \cdot d^\mathrm{h} + 4\ell^2 \boldsymbol{\nabla} d^\mathrm{h} \cdot \boldsymbol{\nabla} d^\mathrm{h}\right) \tag{18}$$

with $\partial d^\mathrm{h}/\partial x_\mathrm{n} = \mathbf{n}_\mathrm{d} \cdot \boldsymbol{\nabla} d^\mathrm{h}$ and $\mathbf{n}_\mathrm{d}^\mathrm{T} \cdot \mathbf{n}_\mathrm{d} = 1$.

In a similar manner we can derive the Heaviside function approximation, $\mathscr{H}_\ell$. Recalling the identity $\mathbf{n}_\mathrm{d} \cdot \nabla \mathscr{H}_{\Gamma_\mathrm{d}} = 2\delta_{\Gamma_\mathrm{d}}$ and Equation (15) we can write

$$\begin{aligned} \mathscr{H}_\ell\left(x_\mathrm{n}\right) = 2\int_0^{x_\mathrm{n}} \frac{1}{2\ell}\exp\left(-\frac{|\varsigma|}{\ell}\right) \mathrm{d}\varsigma = \mathrm{sign}\left(x_\mathrm{n}\right)\left(1 - \exp\left(-\frac{|x_\mathrm{n}|}{\ell}\right)\right) \\ = \mathscr{H}_{\Gamma_d}\left(x_\mathrm{n}\right)\left(1 - 2\ell\delta_\ell\right) \end{aligned} \tag{19}$$

which is identical to the findings by Benvenuti *et al.* [46]. Finally, given $\mathbf{n}_\mathrm{d} \cdot \boldsymbol{\nabla} \mathscr{D}_{\Gamma_\mathrm{d}} = \mathscr{H}_{\Gamma_\mathrm{d}}$,

$$\begin{aligned} \mathscr{D}_\ell\left(x_\mathrm{n}\right) = \int_0^{x_\mathrm{n}} \mathrm{sign}\left(\varsigma\right)\left(1 - \exp\left(-\frac{|\varsigma|}{\ell}\right)\right) \mathrm{d}\varsigma \\ = |x_\mathrm{n}| - \ell\left(1 - \exp\left(-\frac{|x_\mathrm{n}|}{\ell}\right)\right) = \mathscr{D}_{\Gamma_\mathrm{d}}\left(x_\mathrm{n}\right) - \ell\left(1 - 2\ell\delta_\ell\right) \end{aligned} \tag{20}$$

The effect of the length-scale parameter ℓ on the approximated Dirac-delta, Heaviside and signed-distance functions has been presented in Figure 3. As ℓ decreases the solution converges to analytical discrete functions, *i.e.*, $\lim_{\ell\to 0} \mathscr{H}_\ell = \mathscr{H}_{\Gamma_\mathrm{d}}$ and $\lim_{\ell\to 0} \mathscr{D}_\ell = \mathscr{D}_{\Gamma_\mathrm{d}}$.

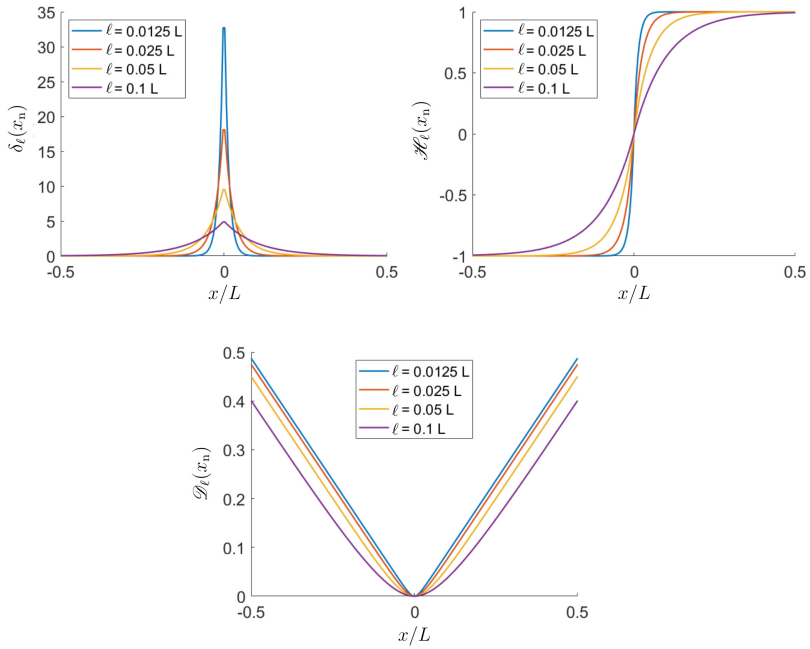

Figure 3: Effect of the phase-field internal length-scale parameter ℓ for the diffused values of Dirac-delta (δ_ℓ), the Heaviside ($\mathscr{H}_\ell$) and the signed-distance ($\mathscr{D}_\ell$) functions. The crack is located at $x = 0$ of a one-dimensional problem with length L

2.2. Constitutive relation at the discontinuity

The potential energy in Equation (14) is written for a non-negligible fracture process zone, which lodges the nonlinear deformations and their gradients. We adopt the cohesive-zone model in the form of tractions at the discontinuity, *i.e.*, $\mathbf{t}_\mathrm{d}\left(\mathbf{x}_\mathrm{c}\right)$ at Γ_d, by means of a the dissipation energy defined

$$\mathcal{G}_\mathrm{f} = \mathcal{G}_\mathrm{f}\left(\llbracket \mathbf{u} \rrbracket(\mathbf{x}_\mathrm{c}), \boldsymbol{\kappa}\right), \quad \forall \mathbf{x}_\mathrm{c} \in \Gamma_\mathrm{d} \tag{21}$$

in terms of the displacement jump, defined in Equation (13), and the history parameter $\boldsymbol{\kappa}$, which stores the maximum experienced displacement jump. In the literature, many options have been proposed for different mechanical behaviours [85], a few of which are explored in our examples. Hereafter, we refer to $\llbracket \mathbf{u} \rrbracket(\mathbf{x}_\mathrm{c})$ simply by $\llbracket \mathbf{u} \rrbracket$, as the notion of the displacement jump is only valid for Γ_d and, therefore, meaningless elsewhere.

Recalling Equation (12) the tractions at Γ_d yield

$$\mathbf{t}_{\mathrm{d}}\left(\llbracket \mathbf{u} \rrbracket, \boldsymbol{\kappa}\right) = \frac{\partial \mathcal{G}_{\mathrm{f}}\left(\llbracket \mathbf{u} \rrbracket, \boldsymbol{\kappa}\right)}{\partial \llbracket \mathbf{u} \rrbracket} \tag{22}$$

in the global coordinate system while the local values of the displacement jump and the traction read

$$\mathbf{t}_{\mathrm{d}}\left(\llbracket \mathbf{u} \rrbracket, \boldsymbol{\kappa}\right) = \mathbf{R}^{\mathrm{T}} \cdot \mathbf{t}_{\mathrm{d}}^{\mathrm{loc}}\left(\llbracket \mathbf{u}^{\mathrm{loc}} \rrbracket, \boldsymbol{\kappa}^{\mathrm{loc}}\right), \quad \llbracket \mathbf{u}^{\mathrm{loc}} \rrbracket = \left\{\llbracket u_{\mathrm{s}}^{\mathrm{loc}} \rrbracket, \llbracket u_{\mathrm{n}}^{\mathrm{loc}} \rrbracket\right\} = \mathbf{R} \cdot \llbracket \mathbf{u} \rrbracket \tag{23}$$

where $\square_{\mathrm{s}}$ and $\square_{\mathrm{n}}$ are the values of $\square$ in the directions tangent and normal to the crack path, respectively. $\mathbf{R}$ denotes the global-local rotation matrix. The Kuhn-Tucker condition is adopted to enforce the irreversibility of the displacement jump,

$$\boldsymbol{f}\left(\llbracket \mathbf{u}^{\mathrm{loc}} \rrbracket, \boldsymbol{\kappa}^{\mathrm{loc}}\right) = \llbracket \mathbf{u}^{\mathrm{loc}} \rrbracket - \boldsymbol{\kappa}^{\mathrm{loc}} \leq 0 \qquad \dot{\boldsymbol{\kappa}}^{\mathrm{loc}} \geq \mathbf{0} \qquad \dot{\boldsymbol{\kappa}}^{\mathrm{loc}} \cdot \boldsymbol{f} = \mathbf{0} \tag{24}$$

where the function $\boldsymbol{f}$ determines the loading/unloading state based on the maximum local opening experienced until the current time, *i.e.*, $\boldsymbol{\kappa}^{\mathrm{loc}} = \max_{\tau \in (-\infty, t]} \llbracket \mathbf{u}^{\mathrm{loc}}(\tau) \rrbracket$.

3. Variational formulation

In line with the cohesive phase-field formulation [39, 42] which adopts the elastic strain, we exploit the second principle of thermodynamics to formulate the diffused version ($\Gamma_{\mathrm{d}} \leftarrow \ell$) of the internal potential energy in Equation (9),

$$0 \leq \dot{\mathfrak{D}} = \boldsymbol{\sigma} : \dot{\boldsymbol{\varepsilon}} - \dot{\psi}^{\mathrm{e}} = \boldsymbol{\sigma} : \left(\dot{\boldsymbol{\varepsilon}}^{\mathrm{e}} + \dot{\boldsymbol{\varepsilon}}^{\mathrm{d}}\right) - \frac{\partial \psi^{\mathrm{e}}}{\partial \boldsymbol{\varepsilon}^{\mathrm{e}}} : \dot{\boldsymbol{\varepsilon}}^{\mathrm{e}} = \boldsymbol{\sigma} : \dot{\boldsymbol{\varepsilon}}^{\mathrm{d}} \tag{25}$$

with the total strain $\boldsymbol{\varepsilon}$ decomposed into elastic and diffused parts, *i.e.* $\boldsymbol{\varepsilon} = \boldsymbol{\varepsilon}^{\mathrm{e}} + \boldsymbol{\varepsilon}^{\mathrm{d}}$. On the other hand, the explicit derivation of the energy dissipation reads

$$\begin{aligned} \dot{\mathfrak{D}} &= \frac{\mathrm{d}\dot{\boldsymbol{\varepsilon}}^{\mathrm{d}}}{\mathrm{d}t} = \frac{\mathrm{d}}{\mathrm{d}t}\left(\mathscr{H}_{\ell} \boldsymbol{\nabla}^{\mathrm{s}} \tilde{\mathbf{u}}^{\mathrm{h}} + \delta_{\ell}\, \mathbf{t}_{\mathrm{d}} \cdot \tilde{\mathbf{u}}^{\mathrm{h}}\right) \\ &= \mathscr{H}_{\ell} \boldsymbol{\nabla}^{\mathrm{s}} \dot{\tilde{\mathbf{u}}}^{\mathrm{h}} + \boldsymbol{\nabla}^{\mathrm{s}} \tilde{\mathbf{u}}^{\mathrm{h}} \frac{\partial \mathscr{H}_{\ell}}{\partial d} \dot{d} + 2\delta_{\ell}\, \mathbf{t}_{\mathrm{d}} \cdot \dot{\tilde{\mathbf{u}}}^{\mathrm{h}} + \mathcal{G}_{\mathrm{f}} \frac{\partial \delta_{\ell}}{\partial d} \dot{d} \end{aligned} \tag{26}$$

where the first and the third terms represent the energy dissipated by further opening of the existing crack, *i.e.* $\dot{\tilde{\mathbf{u}}}$. The second and the fourth terms indicate the energy dissipated through the extension of the cohesive zone by an increment $\dot{d}$. In the cohesive-zone modelling, the newly progressed cohesive zone due to $\dot{d}$ is initially closed, *i.e.* $[\![\mathbf{u}]\!] = \tilde{\mathbf{u}}^{\mathrm{h}} = \mathbf{0}$, and consequently $\mathcal{G}_{\mathrm{f}} = 0$ as well as $\boldsymbol{\nabla}^{\mathrm{s}}\tilde{\mathbf{u}}^{\mathrm{h}} = 0$, which remove the second and the fourth terms. The elastic strain tensor yields

$$\boldsymbol{\varepsilon}^{\mathrm{e}} = \boldsymbol{\varepsilon} - \boldsymbol{\varepsilon}^{\mathrm{d}} = \boldsymbol{\varepsilon} - \mathscr{H}_{\ell}\boldsymbol{\nabla}^{\mathrm{s}}\tilde{\mathbf{u}}^{\mathrm{h}} - 2\delta_{\ell}\left(\tilde{\mathbf{u}}^{\mathrm{h}} \otimes^{\mathrm{s}} \mathbf{n}_{\mathrm{d}}\right) = \boldsymbol{\nabla}^{\mathrm{s}}\hat{\mathbf{u}}^{\mathrm{h}}. \tag{27}$$

Finally, the total potential strain energy function becomes

$$\Psi_{\mathrm{pot}} = \int_{\Omega} \psi^{\mathrm{e}}\left(\boldsymbol{\varepsilon}^{\mathrm{e}}\left(\hat{\mathbf{u}}^{\mathrm{h}}\right)\right)\,\mathrm{d}\Omega + \int_{\Omega} \psi^{\mathrm{d}}\left(\boldsymbol{\varepsilon}^{\mathrm{d}}\left(\tilde{\mathbf{u}}^{\mathrm{h}}, \boldsymbol{\kappa}\right)\right)\,\mathrm{d}\Omega - \mathcal{P}_{\mathrm{ext}}. \tag{28}$$

Plugging $\mathbf{t}_{\mathrm{d}} = \boldsymbol{\sigma}\cdot\mathbf{n}_{\mathrm{d}}$ and Equation (27) into (28)

$$\begin{aligned}\Psi_{\mathrm{pot}} = \int_{\Omega}\left(\frac{1}{2}\boldsymbol{\sigma} : \left(\boldsymbol{\nabla}^{\mathrm{s}}\hat{\mathbf{u}}^{\mathrm{h}} + \mathscr{H}_{\ell}\,\boldsymbol{\nabla}^{\mathrm{s}}\tilde{\mathbf{u}}^{\mathrm{h}}\right) + \delta_{\ell}\,\mathbf{t}_{\mathrm{d}}\left([\![\mathbf{u}]\!], \boldsymbol{\kappa}\right)\cdot\tilde{\mathbf{u}}^{\mathrm{h}}\right)\,\mathrm{d}\Omega \\ - \int_{\Gamma_{\mathrm{t}}} \bar{\mathbf{t}}\cdot\mathbf{u}^{\mathrm{h}}\,\mathrm{d}\Gamma - \int_{\Omega}\bar{\mathbf{b}}\cdot\mathbf{u}^{\mathrm{h}}\,\mathrm{d}\Omega.\end{aligned} \tag{29}$$

Remark 1: Potential strain energy of a discrete Heaviside function
Had we not utilised the regularised description of the Heaviside function and instead only focused on δ_{ℓ}, the energy dissipation in Equation (26) would become

$$\dot{\mathfrak{D}} = \frac{\mathrm{d}\dot{\boldsymbol{\varepsilon}}^{\mathrm{d}}}{\mathrm{d}t} = \frac{\mathrm{d}}{\mathrm{d}t}\left(\delta_{\ell}\,\mathbf{t}_{\mathrm{d}}\cdot\tilde{\mathbf{u}}^{\mathrm{h}}\right) = 2\delta_{\ell}\,\mathbf{t}_{\mathrm{d}}\cdot\dot{\tilde{\mathbf{u}}}^{\mathrm{h}} + \mathcal{G}\frac{\partial\delta_{\ell}}{\partial d}\dot{d}. \tag{30}$$

After applying $[\![\mathbf{u}]\!] = \tilde{\mathbf{u}}^{\mathrm{h}} = \mathbf{0}$ for the newly progressed cohesive zone due to $\dot{d}$, the elastic strain becomes

$$\boldsymbol{\varepsilon}^{\mathrm{e}} = \boldsymbol{\varepsilon} - \boldsymbol{\varepsilon}^{\mathrm{d}} = \boldsymbol{\varepsilon} - 2\delta_{\ell}\left(\tilde{\mathbf{u}}^{\mathrm{h}} \otimes^{\mathrm{s}} \mathbf{n}_{\mathrm{d}}\right) = \boldsymbol{\nabla}^{\mathrm{s}}\hat{\mathbf{u}}^{\mathrm{h}} + \mathscr{H}_{\Gamma_{\mathrm{d}}}\boldsymbol{\nabla}^{\mathrm{s}}\tilde{\mathbf{u}}^{\mathrm{h}} = \boldsymbol{\varepsilon}^{\mathrm{b}}. \tag{31}$$

Finally, according to Equation (28), the total potential strain energy function becomes

$$\begin{aligned}\Psi_{\mathrm{pot}} = \int_{\Omega}\left(\frac{1}{2}\boldsymbol{\sigma} : \left(\boldsymbol{\nabla}^{\mathrm{s}}\hat{\mathbf{u}}^{\mathrm{h}} + \mathscr{H}_{\Gamma_{\mathrm{d}}}\,\boldsymbol{\nabla}^{\mathrm{s}}\tilde{\mathbf{u}}^{\mathrm{h}}\right) + \delta_{\ell}\,\mathbf{t}_{\mathrm{d}}\left([\![\mathbf{u}]\!], \boldsymbol{\kappa}\right)\cdot\tilde{\mathbf{u}}^{\mathrm{h}}\right)\,\mathrm{d}\Omega \\ - \int_{\Gamma_{\mathrm{t}}} \bar{\mathbf{t}}\cdot\mathbf{u}^{\mathrm{h}}\,\mathrm{d}\Gamma - \int_{\Omega}\bar{\mathbf{b}}\cdot\mathbf{u}^{\mathrm{h}}\,\mathrm{d}\Omega.\end{aligned} \tag{32}$$

which is identical to Equation (29) except for $\mathscr{H}_\ell \leftarrow \mathscr{H}_{\Gamma_\mathrm{d}}$, and therefore the same formulation can be used for discrete Heaviside formulation $\mathscr{H}_{\Gamma_\mathrm{d}}$. However, the condition number issue adhered to the discontinuous Heaviside enrichment will certainly remain when the crack divides an element disproportionately. Therefore, remedies identical to those of XFEM, referred in Introduction (Section 1), must be adopted to circumvent the issue.

Remark 2: Retrieving cohesive phase-field formulation given by Verhoosel and de Borst

Verhoosel and de Borst [39] proposed a cohesive phase-field formulation, which was later utilised by other contributions for cohesive fracture [32, 40, 41, 42]. Here we prove that the formulation is a special form of our phase-field-regularised PUM for fracture analysis. We start by rewriting the infinitesimal strain field in Equation (7), while the last term is defined on the displacement jump in Equation (13),

$$\boldsymbol{\varepsilon} = \boldsymbol{\nabla}^\mathrm{s}\mathbf{u}^\mathrm{h} = \boldsymbol{\nabla}^\mathrm{s}\hat{\mathbf{u}}^\mathrm{h} + \mathscr{H}_{\Gamma_\mathrm{d}}\,\boldsymbol{\nabla}^\mathrm{s}\tilde{\mathbf{u}}^\mathrm{h} + \delta_{\Gamma_\mathrm{d}}\,\left(\llbracket\mathbf{u}\rrbracket \otimes^\mathrm{s} \mathbf{n}_{\Gamma_\mathrm{d}}\right)$$

with the elastic strain $\boldsymbol{\varepsilon}^\mathrm{e} = \boldsymbol{\nabla}^\mathrm{s}\hat{\mathbf{u}}^\mathrm{h} + \mathscr{H}_{\Gamma_\mathrm{d}}\,\boldsymbol{\nabla}^\mathrm{s}\tilde{\mathbf{u}}^\mathrm{h}$. Adopting the diffused Dirac-δ given by analytical phase-field solution the elastic strain can be rewritten in terms of the total displacement $\mathbf{u}$ as

$$\boldsymbol{\varepsilon}^\mathrm{e} = \boldsymbol{\nabla}^\mathrm{s}\mathbf{u}^\mathrm{h} - \delta_\ell\,\left(v^\mathrm{h} \otimes^\mathrm{s} \mathbf{n}_\mathrm{d}\right),$$

where $\llbracket\mathbf{u}\rrbracket$ is substituted with v, a one-dimensional auxiliary jump field which is not associated with the displacement field $\mathbf{u}^\mathrm{h}$. Using the newly derived strain field, the total potential energy identical to Verhoosel and de Borst [39] yields,

$$\Psi_\mathrm{pot} = \int_\Omega \left(\frac{1}{2}\boldsymbol{\sigma} : \left(\boldsymbol{\nabla}^\mathrm{s}\mathbf{u}^\mathrm{h} - \delta_\ell\,\left(v^\mathrm{h} \otimes^\mathrm{s} \mathbf{n}_\mathrm{d}\right)\right) + \delta_\ell\,\mathbf{t}_\mathrm{d}\left(v^\mathrm{h}, \boldsymbol{\kappa}\right)\cdot v^\mathrm{h} + \frac{1}{2}\alpha\left|\frac{\partial v^\mathrm{h}}{\partial x_\mathrm{n}}\right|^2\right)\,\mathrm{d}\Omega - \int_{\Gamma_\mathrm{t}} \bar{\mathbf{t}}\cdot\mathbf{u}^\mathrm{h}\,\mathrm{d}\Gamma - \int_\Omega \bar{\mathbf{b}}\cdot\mathbf{u}^\mathrm{h}\,\mathrm{d}\Omega.$$

where the last term in the internal potential energy function, *i.e.*, $\frac{1}{2}\alpha\left|\frac{\partial v^\mathrm{h}}{\partial x_\mathrm{n}}\right|^2$ has been weakly imposed by a penalty factor α to enforce a constant dis-

placement jump in the direction normal to the crack profile [32, 39, 41, 42]

$$\frac{\partial v^{\mathrm{h}}}{\partial x_{\mathrm{n}}} = 0,$$

with $[\![\mathbf{u}]\!](x_{\mathrm{c}}) \approx v^{\mathrm{h}}(x_{\mathrm{c}})$.

In other words, the formulation by Verhoosel and de Borst is retrieved by removing the definition of the total displacement field, $\mathbf{u}^{\mathrm{h}} = \hat{\mathbf{u}}^{\mathrm{h}} + \mathscr{H}_{\Gamma_{\mathrm{d}}}\,\tilde{\mathbf{u}}^{\mathrm{h}}$, from the energy function and utilising additional constraints to compensate for the lack of inherent jump in phase-field models, in contrast to the PUM. Inspired by the formulation proposed by Verhoosel and de Borst, the auxiliary jump field approximation has been upgraded using a first-order Taylor series expansion on the total displacement field $\mathbf{u}$ [40, 86], addressing the absence of any explicit relationship between the displacement and the auxiliary jump field. In our formulation, however, the explicit definition of the displacement jump in Equation (13) obviates the need for the auxiliary jump field v, thereby eliminating the additional constraint imposed by the penalty method and reducing the likelihood of perturbations in equilibrium. Moreover, the resulting jump complies with the PUM, while expansion series are merely approximation tools.

Remark 3: Inclusion of damage-dependent degradation functions
In future developments, the presented formulation can be extended to accommodate a variety of damage-dependent degradation functions. This can help achieve a more straightforward definition of the cohesive phase-field than that given in available degradation-dependent contributions. Moreover, it can help establish a direct relationship between the phase-field variable and the level set function, which enables tracking of the crack by the phase-field and accounting for crack propagation and branching. The latter is a major shortcoming in discrete approaches which can be circumvented by adopting phase-field, while using PUM on the other hand preserves the functionality of the proposed approach with coarse meshes.

3.1. Displacement weak forms

We obtain the admissible displacement field by

$$\mathbf{u}^{\mathrm{h}} = \arg\left\{\inf_{\mathbf{u}^{\mathrm{h}}\in\mathcal{S}_u} \Psi_{\mathrm{pot}}\right\}, \tag{33}$$

where $\mathcal{S}_u = \left\{\mathbf{u}^{\mathrm{h}} | \mathbf{u}^{\mathrm{h}}(\mathbf{x}) = \bar{\mathbf{u}} \;\; \forall \mathbf{x} \in \Gamma_{\mathrm{u}},\; \mathbf{u} \in \mathbb{H}^1(\Omega)\right\}$, and $\mathbb{H}^1$ denotes the first Hilbert space. Taking the variation of the newly derived potential energy functions with respect to the displacement:

$$\partial \Psi_{\mathrm{pot},\,u} = 0 \Longrightarrow \int_{\Omega} \left(\boldsymbol{\sigma} : \left(\boldsymbol{\nabla}^{\mathrm{s}} \delta \hat{\mathbf{u}}^{\mathrm{h}} + \mathscr{H}_{\ell}\, \boldsymbol{\nabla}^{\mathrm{s}} \delta \tilde{\mathbf{u}}^{\mathrm{h}}\right) + 2\delta_{\ell}\, \mathbf{t}_{\mathrm{d}}\left(\llbracket \mathbf{u} \rrbracket, \boldsymbol{\kappa}\right) \cdot \delta \tilde{\mathbf{u}}^{\mathrm{h}}\right) \mathrm{d}\Omega = \int_{\Gamma_{\mathrm{t}}} \bar{\mathbf{t}} \cdot \left(\delta \hat{\mathbf{u}}^{\mathrm{h}} + \mathscr{H}_{\ell} \delta \tilde{\mathbf{u}}^{\mathrm{h}}\right) \mathrm{d}\Gamma + \int_{\Omega} \bar{\mathbf{b}} \cdot \left(\delta \hat{\mathbf{u}}^{\mathrm{h}} + \mathscr{H}_{\ell} \delta \tilde{\mathbf{u}}^{\mathrm{h}}\right) \mathrm{d}\Omega. \quad (34)$$

Equation (34) can be further decomposed into continuous and discontinuous parts

$$\int_{\Omega} \boldsymbol{\sigma} : \boldsymbol{\nabla}^{\mathrm{s}} \delta \hat{\mathbf{u}}^{\mathrm{h}}\, \mathrm{d}\Omega = \int_{\Gamma_{\mathrm{t}}} \bar{\mathbf{t}} \cdot \delta \hat{\mathbf{u}}^{\mathrm{h}}\, \mathrm{d}\Gamma + \int_{\Omega} \bar{\mathbf{b}} \cdot \delta \hat{\mathbf{u}}^{\mathrm{h}}\, \mathrm{d}\Omega \quad (35a)$$

$$\int_{\Omega} \left(\boldsymbol{\sigma} : \mathscr{H}_{\ell}\, \boldsymbol{\nabla}^{\mathrm{s}} \delta \tilde{\mathbf{u}}^{\mathrm{h}} + 2\delta_{\ell}\, \mathbf{t}_{\mathrm{d}}\left(\llbracket \mathbf{u} \rrbracket, \boldsymbol{\kappa}\right) \cdot \delta \tilde{\mathbf{u}}^{\mathrm{h}}\right) \mathrm{d}\Omega = \int_{\Gamma_{\mathrm{t}}} \bar{\mathbf{t}} \cdot \mathscr{H}_{\ell}\, \delta \tilde{\mathbf{u}}^{\mathrm{h}}\, \mathrm{d}\Gamma + \int_{\Omega} \bar{\mathbf{b}} \cdot \mathscr{H}_{\ell}\, \delta \tilde{\mathbf{u}}^{\mathrm{h}}\, \mathrm{d}\Omega \quad (35b)$$

for the continuous and discontinuous equilibrium equations of the mechanical problem. Integrating by parts and adopting the Dirac-delta for the test functions $\delta \hat{\mathbf{u}}$ and $\delta \tilde{\mathbf{u}}$ similar to the collocation method [87], the updated strong forms read

$$\begin{cases} \boldsymbol{\nabla} \cdot \boldsymbol{\sigma}(\mathbf{x}) = \bar{\mathbf{b}} & \mathbf{x} \in \Omega \\ \boldsymbol{\sigma}(\mathbf{x}) \cdot \mathbf{n}_{\mathrm{t}} = \bar{\mathbf{t}} & \mathbf{x} \in \Gamma_{\mathrm{t}} \end{cases} \quad (36a)$$

$$2\delta_{\ell}\left(\mathbf{t}_{\mathrm{d}}\left(\llbracket \mathbf{u} \rrbracket, \boldsymbol{\kappa}\right) - \boldsymbol{\sigma} \cdot \mathbf{n}_{\mathrm{d}}\right) = \mathscr{H}_{\ell}\, \bar{\mathbf{b}} \qquad \mathbf{x} \in \Omega \quad (36b)$$

It is noteworthy that the diffused (continuous) definition of the discontinuity, $\mathscr{H}_{\ell}$, allows for the use of the Dirac-δ as the test function, which is identical to the collocated phase-field [88]. This is due to the requirement of the sifting property of the Dirac-δ at x^*, *i.e.*, $\int_{\Omega} \phi(x) \delta_{\mathrm{Dirac}}\left(x - x^*\right) \mathrm{d}\Omega = \phi\left(x^*\right)$, which is violated if (discontinuous) discrete Heaviside function ($\mathscr{H}_{\Gamma_{\mathrm{d}}}$) is used. For further discussion and alternative solutions, the interested reader is referred to Fathi *et al.* [87].

3.2. Phase-field weak form

Taking the variation of the newly derived potential energy function in Equation (29) with respect to the phase-field variable d yields

$$\begin{aligned}\partial\Psi_{\mathrm{pot,\,d}} = 0 \Longrightarrow & \int_{\Omega} \left(\boldsymbol{\sigma} : \partial\mathscr{H}_{\ell,\,d}\,\boldsymbol{\nabla}^{\mathrm{s}}\tilde{\mathbf{u}}^{\mathrm{h}} + 2\,\partial\delta_{\ell,\,d}\,\mathbf{t}_{\mathrm{d}}\left(\llbracket\mathbf{u}\rrbracket, \boldsymbol{\kappa}\right)\cdot\tilde{\mathbf{u}}^{\mathrm{h}}\right)\,\mathrm{d}\Omega \\ & = \int_{\Gamma_{\mathrm{t}}} \partial\mathscr{H}_{\ell,\,d}\left(\bar{\mathbf{t}}\cdot\tilde{\mathbf{u}}^{\mathrm{h}}\right)\,\mathrm{d}\Gamma + \int_{\Omega}\partial\mathscr{H}_{\ell,\,d}\left(\bar{\mathbf{b}}\cdot\tilde{\mathbf{u}}^{\mathrm{h}}\right)\,\mathrm{d}\Omega\end{aligned} \tag{37}$$

with

$$\partial\delta_{\ell,\,d} = \frac{\delta d^{\mathrm{h}}\cdot d^{\mathrm{h}}}{2\ell} + 2\ell\,\boldsymbol{\nabla}\delta d^{\mathrm{h}}\cdot\boldsymbol{\nabla}d^{\mathrm{h}}, \tag{38a}$$

$$\partial\mathscr{H}_{\ell,\,d} = -2\ell\,\mathscr{H}_{\Gamma_{\mathrm{d}}}\,\partial\delta_{\ell,\,d} = -\mathscr{H}_{\Gamma_{\mathrm{d}}}\,\left(\delta d^{\mathrm{h}}\cdot d^{\mathrm{h}} + 4\ell^2\,\boldsymbol{\nabla}\delta d^{\mathrm{h}}\cdot\boldsymbol{\nabla}d^{\mathrm{h}}\right). \tag{38b}$$

By applying the divergence theorem on the external traction ($\bar{\mathbf{t}} = \boldsymbol{\sigma}\cdot\mathbf{n}_{\mathrm{d}}$) term the final form, after some rewriting, becomes [39]

$$\begin{aligned}&\partial\Psi_{\mathrm{pot},\,d} = 0 \Longrightarrow \\ &\int_{\Omega}\partial\delta_{\ell,\,d}\underbrace{\left(2\ell\mathscr{H}_{\Gamma_{\mathrm{d}}}\left(\boldsymbol{\sigma} : -\boldsymbol{\nabla}^{\mathrm{s}}\tilde{\mathbf{u}}^{\mathrm{h}} + \boldsymbol{\nabla}\cdot\left(\boldsymbol{\sigma}\cdot\tilde{\mathbf{u}}^{\mathrm{h}}\right) + \bar{\mathbf{b}}\cdot\tilde{\mathbf{u}}^{\mathrm{h}}\right) + 2\,\mathbf{t}_{\mathrm{d}}\left(\llbracket\mathbf{u}\rrbracket_{\ell}, \boldsymbol{\kappa}\right)\cdot\tilde{\mathbf{u}}^{\mathrm{h}}\right)}_{\text{constant}\neq 0}\,\mathrm{d}\Omega = 0 \\ &\Longrightarrow \int_{\Omega}\partial\delta_{\ell,\,d}\,\mathrm{d}\Omega = 0\end{aligned} \tag{39}$$

In this paper, the Dirichlet constraints of the phase-field for pre-existing cracks, *i.e.* $d^{\mathrm{h}}|_{\Gamma_{\mathrm{d}}} = 1$ in Equation (16), are imposed weakly [29, 31, 39]. This obviates manipulating the mesh in order to accommodate the Dirichlet constraints [32]. Applying these conditions in the weak form leads to

$$\int_{\Omega}\left(\delta d^{\mathrm{h}}\,d^{\mathrm{h}} + 4\ell^2\,\boldsymbol{\nabla}\delta d^{\mathrm{h}}\cdot\boldsymbol{\nabla}d^{\mathrm{h}}\right)\,\mathrm{d}\Omega + 2\ell c_0\int_{\Omega}\delta d^{\mathrm{h}}\left(d^{\mathrm{h}} - 1\right)\delta_0\left(x_{\mathrm{n}}\right)\,\mathrm{d}\Omega = 0 \tag{40}$$

where c_0 is the non-negative coefficient weighing the weak imposition of the Dirichlet constraint term [39]. Rewriting Equation (40) leads to

$$\int_\Omega \left((1+\mathcal{F})\delta d^{\mathrm{h}} \cdot d^{\mathrm{h}} + 4\ell^2 \boldsymbol{\nabla}\delta d^{\mathrm{h}} \cdot \boldsymbol{\nabla} d^{\mathrm{h}}\right) \, \mathrm{d}\Omega = \int_\Omega \mathcal{F}\delta d^{\mathrm{h}} \, \mathrm{d}\Omega \tag{41}$$

with $\mathcal{F}$, the driving force [39],

$$\mathcal{F} = 2\ell c_0 \, \delta_0(x_{\mathrm{n}}), \quad \delta_0(x_{\mathrm{n}}) = \begin{cases} \frac{2}{h}\left(1 - \frac{2|x_{\mathrm{n}}|}{h}\right) & \frac{-h}{2} \leq x_{\mathrm{n}} \leq \frac{h}{2} \\ 0 & \text{otherwise} \end{cases}, \tag{42}$$

where h indicates the mesh size.

4. Discretisation

Herein, we focus on finite element implementation by discretising the weak forms, in which the domain Ω is subdivided into non-overlapping smaller sections, also known as elements

$$\Omega = \bigcup_{e}^{n_{\mathrm{elm}}} \Omega^e. \tag{43}$$

While Lagrange polynomials are typically used as the set of basis functions for the customary finite element analysis [89, 90], we adopt spline technology used in isogeometric analysis (IGA) [70], particularly Non-uniform rational B-splines (NURBS).

4.1. Bézier-extraction-based NURBS

We construct a NURBS surface on a univariate B-spline basis function, *i.e.* $\mathbf{N}^{\text{B-spline}}$,

$$\mathbf{S}(\boldsymbol{\xi}) = \sum_{k=1}^{n_{\mathrm{IGA}}} \mathbf{N}_k(\boldsymbol{\xi}) \, \mathbf{P}_k, \quad N_{k,p}(\xi) = \frac{w_k \, N_{k,p}^{\text{B-spline}}}{\mathcal{W}(\xi)}. \tag{44}$$

that is defined by the Cox-de Boor formula[89] with $\mathcal{W}(\xi) = \sum_{k=1}^{n} N_k^{\text{B-spline}}(\xi) w_k$ which utilise the weights $\mathbf{w}$, and p denotes the order of the underlying knot vector. n_{IGA} is the number of control points $\mathbf{P}$.

Use of Bézier extraction provides a direct transformation from physical space to the parametric domain identical to the finite element data-structure. Therefore, we use the Bézier extraction operator $\mathbf{C}$

$$\left(\mathbf{N}^{\text{B-spline}}\right)^e = \mathbf{C}^e \boldsymbol{\mathcal{B}}. \tag{45}$$

The superscript "e" denotes the element index, which is different from "e" used for the elastic term, and $\boldsymbol{\mathcal{B}}$ indicates a univariate Bernstein polynomial within the input domain $[-1\ 1]$,

$$\mathcal{B}_{k,p}(\xi) = \frac{1}{2}(1-\xi)\mathcal{B}_{k,p-1}(\xi) + \frac{1}{2}(1+\xi)\mathcal{B}_{k-1,p-1}(\xi) \tag{46a}$$

$$\mathcal{B}_{1,0}(\xi) \equiv 1 \tag{46b}$$

$$\mathcal{B}_{k,p}(\xi) \equiv 0 \qquad \text{if} \quad k < 1 \quad \text{or} \quad k > p+1. \tag{46c}$$

Generalisation to multi dimensions is possible via tensor product.

4.2. Phase-field discretisation

The phase-field weak form in Equation (41) is now discretised using finite elements

$$d^{\text{h}} = \mathbf{N}_d\, \hat{\mathbf{d}}, \tag{47}$$

where $\hat{\mathbf{d}}$ denotes the set of phase-field DOFs and $\mathbf{N}_d$ is the NURBS set of basis functions utilised for phase-field. Accordingly, the phase-field weak form defined in Equation (41) leads to

$$\overbrace{\int_\Omega \left[(1+\mathcal{F})\mathbf{N}_d^{\text{T}}\mathbf{N}_d + 4\ell^2\mathbf{B}_d^{\text{T}}\mathbf{B}_d\right]\, \mathrm{d}\Omega\, \hat{\mathbf{d}}}^{\mathbf{f}_{\hat{d}}^{\text{int}}} \;=\; \overbrace{\int_\Omega \mathcal{F}\mathbf{N}_d^{\text{T}}\, \mathrm{d}\Omega}^{\mathbf{f}_{\hat{d}}^{\text{ext}}} \tag{48}$$

where $\mathbf{B}$ contains the derivatives of the shape function, and $\mathcal{F}$ is given in Equation (42). The tangent term corresponding to this equation yields

$$\mathbf{K}_{\hat{d}\hat{d}} = \frac{\partial \mathbf{f}_{\hat{d}}^{\text{int}}}{\partial \hat{\mathbf{d}}} = \int_\Omega \left((1+\mathcal{F})\mathbf{N}_d^{\text{T}}\mathbf{N}_d + 4\ell^2\mathbf{B}_d^{\text{T}}\mathbf{B}_d\right)\, \mathrm{d}\Omega. \tag{49}$$

The regularised Dirac-δ in Equation (18) is also discretised as

$$\delta_\ell = \hat{\mathbf{d}}^{\text{T}}\left(\frac{1}{4\ell}\mathbf{N}_d^{\text{T}}\mathbf{N}_d + \ell\mathbf{B}_d^{\text{T}}\mathbf{B}_d\right)\hat{\mathbf{d}}. \tag{50}$$

A convergence study on Equation (48) for the problem of dimensions $L \times W = 2 \times 1$–uniformly discretised into elements of size h–is presented in Figure 4, where the Γ-error is defined

$$\Gamma\text{-error} = \int_{\Omega} \delta_\ell \, \mathrm{d}\Omega - \Gamma_{\mathrm{d}} = W \left(\int_{-L/2}^{L/2} \delta_\ell \, \mathrm{d}x_n - 1 \right) \tag{51}$$

with $\Gamma_{\mathrm{d}} = W$ for this example. Moreover, L^2 norm and H^1 semi-norm errors are used in this article as well,

$$\mathrm{L}^2\text{-error} = \left(\int_{\Omega} \left(\bullet^{\mathrm{h}} - \bullet_{\mathrm{exct}} \right)^2 \mathrm{d}\Omega \right)^{\frac{1}{2}} \quad \mathrm{H}^1\text{-error} = \left(\int_{\Omega} \left(\frac{\partial \bullet^{\mathrm{h}}}{\partial \mathbf{x}} - \frac{\partial \bullet_{\mathrm{exct}}}{\partial \mathbf{x}} \right)^2 \mathrm{d}\Omega \right)^{\frac{1}{2}} \tag{52}$$

The results for the linear and quadratic NURBS discretisations are separated, in which L^2 and Γ errors are explored for different scenarios. L^2 norm error compares the estimates with exact phase-field values $d_\ell = \exp\left(-\frac{|x_{\mathrm{n}}|}{2\ell}\right)$, and Γ-error assesses the Dirac-δ identity which is directly used in the regularisation, *i.e.*, $\delta_\ell = \frac{1}{2\ell} \exp\left(-\frac{|x_{\mathrm{n}}|}{\ell}\right)$. First, we explore the errors against $\mathbb{h}$-refinement for different length-scales at the fixed $c_0 = 9$. While the L^2-errors in Figures 4A and G recommend larger length-scales, insensitivity of the Γ-errors in D and J are evident (except for the anomaly observed for $\ell = h/20$ in J). The results corresponding to different c_0s, at the fixed $\ell = 2h/15$ reveal different prescriptions for coarse and fine meshes. Nevertheless, $\forall c_0 \in \{8, 9, 10\}$ an approximately stable behaviour is observed for all discretisations, which is supported by both L^2 and Γ errors presented in Figures 4B, E, H and K. To consider c_0 and ℓ simultaneously, three-dimensional surfaces are presented for a fixed discretisation (25 elements) in Figure 4. Blue and orange surfaces indicate linear and quadratic NURBS, respectively. L^2- and Γ-error surfaces are sliced at particular length-scales in the subplots C, F, I and L for better clarity. It is worth mentioning that, although the above-mentioned optimum values for c_0 proved to be effective in this work, c_0 might generally be expected to be problem-dependent.

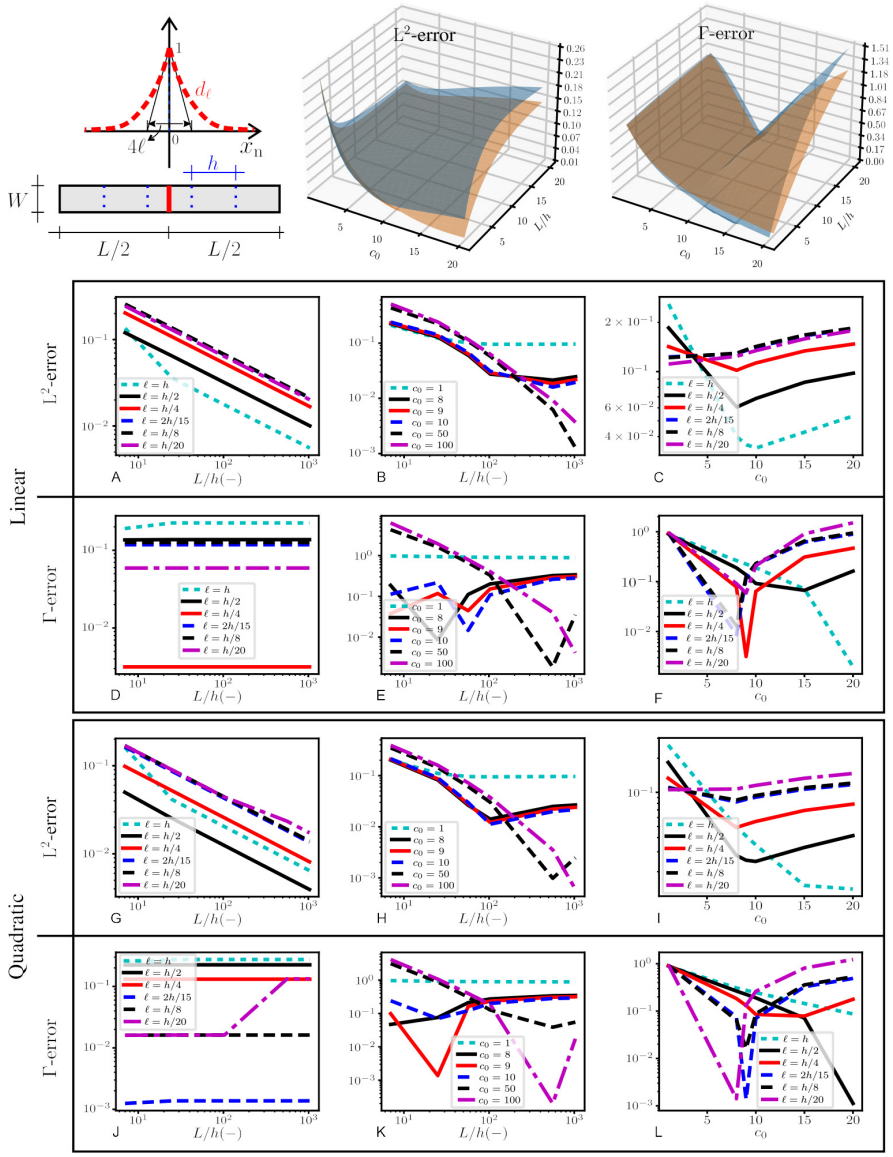

Figure 4: Sensitivity analysis of the phase-field solution with respect to the length-scale parameter ℓ and the constant c_0. L^2-norm error with respect to the exact phase-field solution and Γ-error are reported for different ℓs in A, D, G and J, adopting $c_0 = 9$. B, E, H and K explore different c_0s in the form of L^2 and Γ errors when the constant length-scale $\ell = 2h/15$ is adopted for 25 elements. To explore the effect of c_0 and ℓ simultaneously, L^2 and Γ errors are shown by three-dimensional surfaces on the top, where blue and orange surfaces indicate linear and quadratic NURBS shape functions, respectively. The surfaces are further sliced for various ℓs in C, F, I and L.

4.3. Displacement discretisation

Next, we discretise the displacement field $\mathbf{u}^{\mathrm{h}}$ for a regularised extended finite element analysis using a Bubnov-Galerkin approach as

$$\mathbf{u}^{\mathrm{h}} = \hat{\mathbf{u}}^{\mathrm{h}} + \mathscr{H}_\ell \tilde{\mathbf{u}}^{\mathrm{h}} = \mathbf{N}_{\hat{u}}\,\hat{\mathbf{u}} + \mathscr{H}_\ell \mathbf{N}_{\tilde{u}}\,\tilde{\mathbf{u}}. \tag{53}$$

Discretisation of the governing weak form in Equations (35a) and (35b) yields

$$\overbrace{\int_\Omega \mathbf{B}_{\hat{u}}^{\mathrm{T}}\,\boldsymbol{\sigma}\,\mathrm{d}\Omega}^{\mathbf{f}_{\hat{u}}^{\mathrm{int}}} = \overbrace{\int_{\Gamma_t} \mathbf{N}_{\hat{u}}^{\mathrm{T}}\,\bar{\mathbf{t}}\,\mathrm{d}\Gamma + \int_\Omega \mathbf{N}_{\hat{u}}^{\mathrm{T}}\,\bar{\mathbf{b}}\,\mathrm{d}\Omega}^{\mathbf{f}_{\hat{u}}^{\mathrm{ext}}} \tag{54a}$$

$$\overbrace{\int_\Omega \left((\mathbf{B}_{\tilde{u}}^{\mathrm{enr}})^{\mathrm{T}}\,\boldsymbol{\sigma} + 2\delta_\ell\,\mathbf{N}_{\tilde{u}}^{\mathrm{T}}\,\mathbf{R}^{\mathrm{T}}\,\mathbf{t}_{\mathrm{d}}^{\mathrm{loc}} \right)\,\mathrm{d}\Omega}^{\mathbf{f}_{\tilde{u}}^{\mathrm{int}}} = \overbrace{\int_{\Gamma_t} (\mathbf{N}_{\tilde{u}}^{\mathrm{enr}})^{\mathrm{T}}\,\bar{\mathbf{t}}\,\mathrm{d}\Gamma + \int_\Omega (\mathbf{N}_{\tilde{u}}^{\mathrm{enr}})^{\mathrm{T}}\,\bar{\mathbf{b}}\,\mathrm{d}\Omega}^{\mathbf{f}_{\tilde{u}}^{\mathrm{ext}}} \tag{54b}$$

with $\square^{\mathrm{enr}} = \mathscr{H}_\ell \square$. The equations are then linearised in a Newton-Raphson iterative scheme with the tangent terms

$$\mathbf{K} = \begin{bmatrix} \mathbf{K}_{\hat{u}\hat{u}}^{\Omega} & \mathbf{K}_{\hat{u}\tilde{u}}^{\Omega} \\ \mathbf{K}_{\tilde{u}\hat{u}}^{\Omega} & \mathbf{K}_{\tilde{u}\tilde{u}}^{\Omega} \end{bmatrix} \tag{55}$$

where

$$\mathbf{K}_{\hat{u}\hat{u}}^{\Omega} = \frac{\partial \mathbf{f}_{\hat{u}}^{\mathrm{int}}}{\partial \hat{\mathbf{u}}} = \int_\Omega \mathbf{B}_{\hat{u}}^{\mathrm{T}}\,\mathbb{C}\,\mathbf{B}_{\hat{u}}\,\mathrm{d}\Omega \tag{56a}$$

$$\mathbf{K}_{\hat{u}\tilde{u}}^{\Omega} = \left(\mathbf{K}_{\tilde{u}\hat{u}}^{\Omega}\right)^{\mathrm{T}} = \frac{\partial \mathbf{f}_{\hat{u}}^{\mathrm{int}}}{\partial \tilde{\mathbf{u}}} = \left(\frac{\partial \mathbf{f}_{\tilde{u}}^{\mathrm{int}}}{\partial \hat{\mathbf{u}}}\right)^{\mathrm{T}} = \int_\Omega \mathbf{B}_{\hat{u}}^{\mathrm{T}}\,\mathbb{C}\,\mathbf{B}_{\tilde{u}}^{\mathrm{enr}}\,\mathrm{d}\Omega \tag{56b}$$

$$\mathbf{K}_{\tilde{u}\tilde{u}}^{\Omega} = \frac{\partial \mathbf{f}_{\tilde{u}}^{\mathrm{int}}}{\partial \tilde{\mathbf{u}}} = \int_\Omega \left((\mathbf{B}_{\tilde{u}}^{\mathrm{enr}})^{\mathrm{T}}\,\mathbb{C}\,\mathbf{B}_{\tilde{u}}^{\mathrm{enr}} + 4\delta_\ell\,\mathbf{N}_{\tilde{u}}^{\mathrm{T}}\,\mathbf{R}^{\mathrm{T}}\,\frac{\partial \mathbf{t}_{\mathrm{d}}^{\mathrm{loc}}}{\partial [\![\mathbf{u}]\!]}\,\mathbf{R}\,\mathbf{N}_{\tilde{u}} \right)\,\mathrm{d}\Omega. \tag{56c}$$

Noteworthy is that the displacement jump in Equation (13) is directly used in deriving the stiffness term presented in Equation (56c).

5. Implementation aspects

Herein, we mention the main implementation requirements for a PUM regularised by phase-field for fracture analysis. The staggered solution scheme, solving phase-field first to determine the state of the crack and then assessing the balance of momentum for the determined crack state, is the well-established choice in phase-field models [26, 30, 39], which is also adopted here for the numerical solution of phase-field.

5.1. Compatibility enforcement

Compatibility enforcement is a necessary component in extended finite element analysis, which has been studied for different aspects of isogeometric analysis in finite element [73, 74, 84] and meshfree approaches [76]. Two numerical techniques have usually been adopted in the extended framework, the shifting and the blending. The shifting localises the enriched field into a narrow band in the directions perpendicular to the crack profile, mitigating the error arisen from the additional enhanced term at nodal/control points. Rewriting the shifted version of the displacement field in Equation (3) reads

$$u^{\mathrm{h,SH}}(\mathbf{x}) = \sum_{i\in\mathcal{I}} N_{\hat{u}_i}(\mathbf{x})\,\hat{u}_i + \sum_{i\in\mathcal{I}^{\mathrm{enr}}} \underbrace{\left(\mathscr{H}_{\Gamma_{\mathrm{d}}}\left(x_{\mathrm{n}}\right) - \mathscr{H}_{\Gamma_{\mathrm{d}}}\left(x_{\mathrm{n}_i}\right)\right)}_{\mathscr{H}^{\mathrm{SH}}_{\Gamma_{\mathrm{d}}}(x_{\mathrm{n}})} N_{\tilde{u}_i}(\mathbf{x})\,\tilde{u}_i. \tag{57}$$

where $\mathcal{I}$ denotes the set of all control points in the domain and $\mathcal{I}^{\mathrm{enr}}$ indicates the enriched subset of control points, *i.e.*, $\mathcal{I}^{\mathrm{enr}} \subset \mathcal{I}$. Figure 5 illustrates $\mathscr{H}^{\mathrm{SH}}_{\Gamma_{\mathrm{d}}}\left(x_{\mathrm{n}}\right)$. It is noted that a $\mathcal{C}^0$-continuity at element boundaries, accompanied with the shifting technique, guarantees the enriched field confined by the cracked elements boundaries only. This can be either achieved by the use of Lagrange polynomials within a customary finite element framework or by knot insertion in isogeometric analysis.[71]

The blending technique, on the other hand, removes the effect of discontinuity at crack front arisen from the inter-element share of the control points. This is imposed by employing a Heaviside step function, $\mathscr{H}^{\mathrm{BL}}_{\Gamma_{\mathrm{d}}} = 0$ in front of the crack tip and $\mathscr{H}^{\mathrm{BL}}_{\Gamma_{\mathrm{d}}} = 1$ otherwise, in XIGA [74]. Applying the blending technique to the shifted displacement field yields

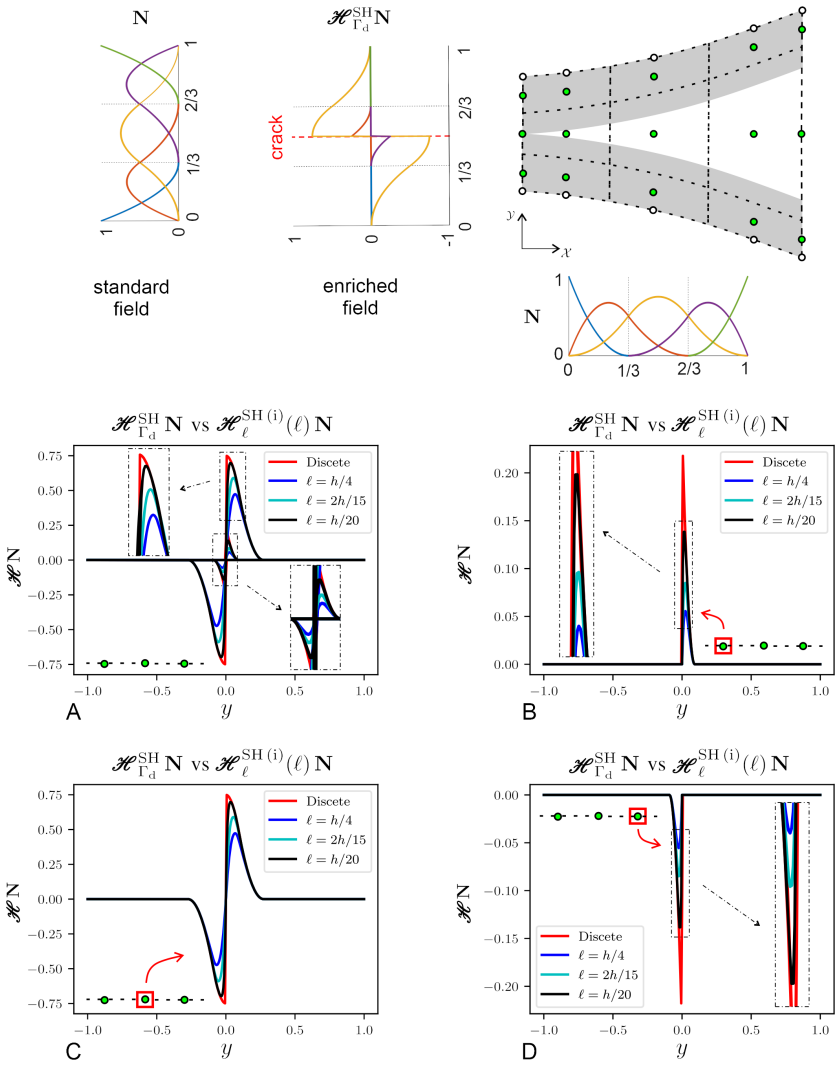

Figure 5: Shifting technique comparison between the discrete and the regularised Heaviside functions, $\mathscr{H}^{\mathrm{SH}}_{\Gamma_{\mathrm{d}}}$ and $\mathscr{H}^{\mathrm{SH\,(i)}}_{\ell}$. Shifting technique is shown for $\mathscr{H}^{\mathrm{SH}}_{\Gamma_{\mathrm{d}}}$ in a Mode-I fracture of quadratic NURBS, following the XIGA's enrichment recipe (the green circles denote the enriched control points). Univariate standard and enriched fields are illustrated for the discontinuity in the $\mathcal{Y}$-direction, while the medium is continuous along the $\mathcal{X}$-direction. The results of the shifting techniques for an eleven-element discretisation are compared for different length-scales in A. For further clarification, the set of shifted basis functions associated with the enriched control points are represented separately in B, C and D.

$$u^{\mathrm{h,SH}}(\mathbf{x}) = \sum_{i\in\mathcal{I}} N_{\hat{u}_i}(\mathbf{x})\,\hat{u}_i + \sum_{i\in\mathcal{I}^{\mathrm{enr}}} \mathscr{H}^{\mathrm{BL}}_{\Gamma_\mathrm{d}}(x_\mathrm{s})\,\underbrace{\left(\mathscr{H}_{\Gamma_\mathrm{d}}(x_\mathrm{n}) - \mathscr{H}_{\Gamma_\mathrm{d}}(x_{\mathrm{n}_i})\right)}_{\mathscr{H}^{\mathrm{SH}}_{\Gamma_\mathrm{d}}(x_\mathrm{n})} N_{\tilde{u}_i}(\mathbf{x})\,\tilde{u}_i. \tag{58}$$

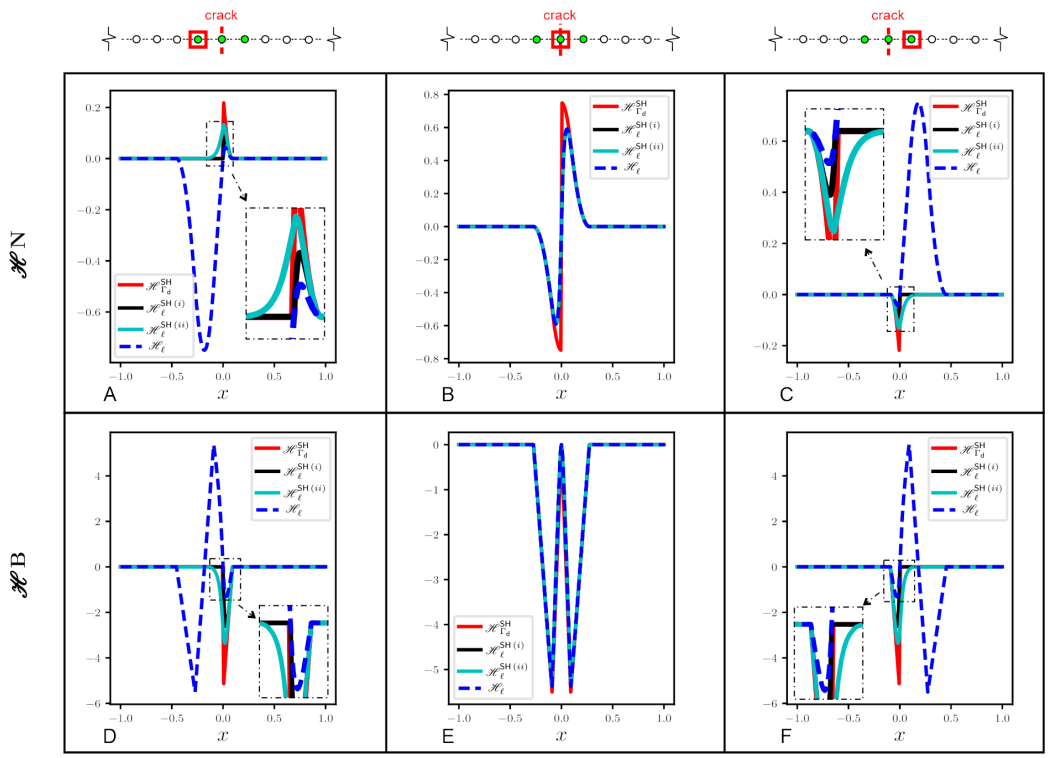

Figure 6: Comparison among the diffused Heaviside function and its shifted candidates. Enriched set of shape functions (A, B and C) and and their gradients (D, E and F) are presented for the enriched control points, indicated by green circles, individually.

5.1.1. Regularised compatibility enforcement technique

Now we derive compatibility enforcement on the regularised Heaviside function in Equation (19).

$$u^{\mathrm{h}}_{\ell}(\mathbf{x}) = \sum_{i\in\mathcal{I}} N_{\hat{u}_i}(\mathbf{x})\,\hat{u}_i + \sum_{i\in\mathcal{I}^{\mathrm{enr}}} \underbrace{\mathscr{H}_{\Gamma_\mathrm{d}}(x_\mathrm{n})\,(1-2\ell\delta_\ell)}_{\mathscr{H}_\ell(x_\mathrm{n})} N_{\tilde{u}_i}\,\tilde{u}_i \tag{59}$$

We employ the shifting technique for the diffused displacement field, leading to two candidates for the shifted, regularised, Heaviside functions:

$$u_\ell^{\mathrm{h,\,SH\,(i)}}(\mathbf{x}) = \sum_{i\in\mathcal{I}} N_{\hat{u}_i}(\mathbf{x})\,\hat{u}_i + \sum_{i\in\mathcal{I}^{\mathrm{enr}}} \underbrace{\left(\mathscr{H}_{\Gamma_\mathrm{d}}\left(x_\mathrm{n}\right) - \mathscr{H}_{\Gamma_\mathrm{d}}\left(x_{\mathrm{n}_j}\right)\right)\left(1-2\ell\delta_\ell\right)}_{\mathscr{H}_\ell^{\mathrm{SH\,(i)}}(x_\mathrm{n})} N_{\tilde{u}_i}\,\tilde{u}_i \tag{60}$$

and

$$u_\ell^{\mathrm{h,\,SH\,(ii)}}(\mathbf{x}) = \sum_{i\in\mathcal{I}} N_{\hat{u}_i}(\mathbf{x})\,\hat{u}_i + \sum_{i\in\mathcal{I}^{\mathrm{enr}}} \underbrace{\left(\mathscr{H}_{\Gamma_\mathrm{d}}\left(x_\mathrm{n}\right)\left(1-2\ell\delta_\ell\right) - \mathscr{H}_{\Gamma_\mathrm{d}}\left(x_{\mathrm{n}_i}\right)\left(1-2\ell\delta_{\ell_i}\right)\right)}_{\mathscr{H}_\ell^{\mathrm{SH\,(ii)}}(x_\mathrm{n})} N_{\tilde{u}_i}\,\tilde{u}_i. \tag{61}$$

To confirm $\lim_{\ell\to 0}\mathscr{H}_\ell^{\mathrm{SH}} = \mathscr{H}_{\Gamma_\mathrm{d}}^{\mathrm{SH}}$, a comparison has been made between $\mathscr{H}_{\Gamma_\mathrm{d}}^{\mathrm{SH}}$ and $\mathscr{H}_\ell^{\mathrm{SH\,(i)}}$ in Figure 5. Next, another comparison is made between the Heaviside functions candidates, *i.e.*, $\left\{\mathscr{H}_{\Gamma_\mathrm{d}}^{\mathrm{SH}}, \mathscr{H}_\ell, \mathscr{H}_\ell^{\mathrm{SH\,(i)}}, \mathscr{H}_\ell^{\mathrm{SH\,(ii)}}\right\}$ in Figure 6. Shifting candidates are further applied to the equations in Section 4.3 by simply replacing the Heaviside function with the shifted candidates, *i.e.*, $\mathscr{H}_\ell \leftarrow \mathscr{H}_\ell^{\mathrm{SH\,(i)}} \vee \mathscr{H}_\ell^{\mathrm{SH\,(ii)}}$.

As previously discussed, the inter-element share of the control points undesirably extends the discontinuous field to the crack front. This has been prevented through the blending technique used for sharp cracks, *e.g.*, $\mathscr{H}_{\Gamma_\mathrm{d}}^{\mathrm{BL}}$ in Equation (58), to retrieve the intact behaviour of crack front. For the regularised formulation, however, the contribution of the discontinuous (enriched) field at the crack front, see the purple shade in Figure 7, is disregarded, rendering use of additional Heaviside step function redundant. Consequently, the notion of displacement jump becomes meaningless at the crack front (see the purple shade in Figure 7), leading to cohesive traction elimination.

5.2. Integration and crack extension direction

Greville abscissae are naturally used in IGA integration of intact bodies. Following the comprehensive study on extended isogeometric collocation method, however, they are proven incompatible with PUM for fracture analysis, as enough integration points are needed at cracked sections for the Heaviside function evaluation [87]. Hence, Gauss quadrature is used as the standard integration scheme in this article. It is worth noting that neither quadrature sub-cell strategy, such as tesselation typically used in XFEM, nor equivalent polynomial approximants [46] are utilised in this study. Instead,

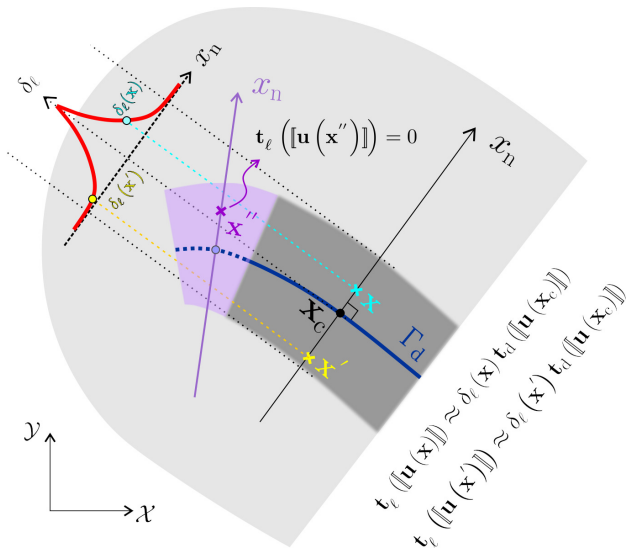

Figure 7: Regularised evaluation of cohesive tractions. Points are first projected onto the crack path (the solid blue line) where the displacement jump $[\![\mathbf{u}]\!]$ is explicitly defined via PUM. Accordingly, points $\mathbf{x}$ and $\mathbf{x}'$ share the same central point on the crack path $\mathbf{x}_\mathrm{c}$, therefore sharing the displacement jump and cohesive traction which is finally diffused with their respective δ_ℓ values. Considering a fictitious crack extension profile distinguished by the dotted blue line, cohesive tractions at $\mathbf{x}''$ are disregarded, as points in front of the crack tip, indicated by the purple shade, are intact.

a 9×9 standard Gauss quadrature for fixed grid points are considered here, see Figure 8, unless stated otherwise. This automatically forms a band of improved integration around the crack path, as shown in Figure 8, which becomes narrower with mesh refinement. Next, employing phase-field has relaxed the line integration typically needed for cohesive-zone discrete fracture models, which subsequently eliminates point projection [74, 91]. As an alternative, the displacement jump at a given point $\mathbf{x}$ is evaluated at the closest point on the crack profile, *i.e.*, $\mathbf{x}_\mathrm{c} = \operatorname{argmin}\left(\|\mathbf{x}^* - \mathbf{x}\|\right)$ with $\mathbf{x}^* \in \Gamma_\mathrm{d}$, see Figure 7. This is then weighted by the value of $\delta_\ell(\mathbf{x})$, identical to the constant displacement jump at the diffused region used in Verhoosel and de Borst [39]; however, without additional constraint enforced on the displacement jump.

Crack initiation and propagation are introduced in the same manner as in extended finite element analysis, through the level set technique and enrichment. In this regard, our proposed approach offers no improvement over the classical extended finite element analysis. However, it can still be improved in terms of crack initiation and tracking by incorporating a degradation func-

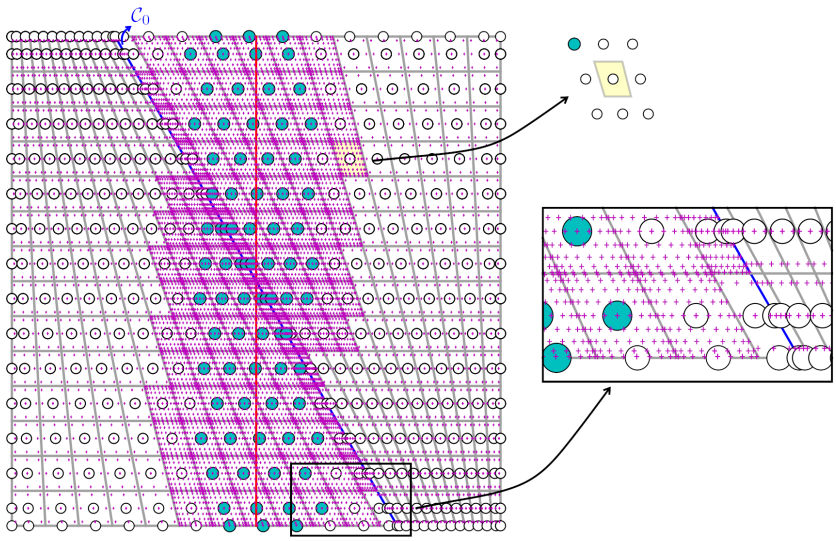

Figure 8: Integration point distribution. For a NURBS of orders p and q in the $\mathcal{X}$ and $\mathcal{Y}$ directions, a normal $(p+1) \times (q+1)$ Gauss quadrature is utilised for non-enriched elements, while a 9×9 is adopted for the elements with enriched control points, see the yellow element with one enriched point. Here, the integration scheme is shown for the quadratic NURBS, *i.e.*, $p = q = 2$. The green circles denote the enriched control points, the red line indicate the crack profile, and a $\mathcal{C}_0$-continuity is introduced through knot insertion and is illustrated by the blue line.

tion — as discussed in Remark 3 — which would enable automated crack path monitoring via a phase-field-dependent level-set function. This will be the subject of our future work.

In this article, the crack extension direction is determined by the nonlocally-averaged maximum principal stress at the crack tip — an approach commonly used in the extended finite element analysis. The reason behind the non-local averaging [92] is the stress oscillations around the crack tip [24, 74], despite the improvements in stress estimation by spline technologies. Crack nucleation occurs when the majority of the points on the potential crack extension satisfy the evolution criterion on the ultimate tensile strength t_{u}, *i.e.*, $t_{\mathrm{d}} \geq t_{\mathrm{u}}$. Therefore, no improvement is made here regarding the extension direction and propagation in comparison with the extended finite element analysis. An alternative could be treating the phase-field as damage variable, beyond a mere regularisation term, by considering a degradation function, which will be explored in our future work.

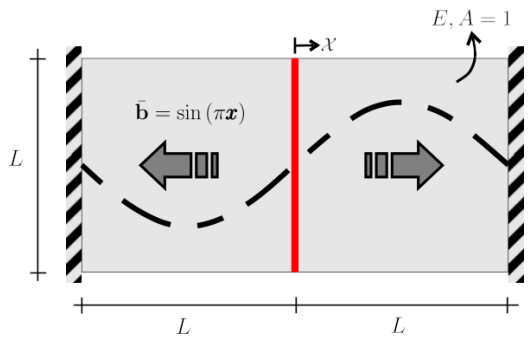

Figure 9: Plate subjected to sinusoidal body forces with a traction-free middle-crack.

6. Numerical examples

The efficacy of the proposed formulation is examined here at the hand of multiple numerical examples for stationary and propagating fractures. Herein, 1 element is assumed in the $\mathcal{Y}$-direction, unless two values are reported in the format $\bigcirc \times \square$, where $\bigcirc$ and $\square$ indicate the number of elements used in the $\mathcal{X}$ and $\mathcal{Y}$ directions, respectively.

6.1. Traction-free stationary crack

A mode-I traction-free fracture is explored in a plate subjected to sinusoidal body forces as our first example, see Figure 9. Young's modulus of $E = 1$ and the cross-section area $A = 1$ are assumed. The exact solution reads:

$$u^{\mathrm{ex}} = \begin{cases} \frac{1}{\pi^2} \sin(\pi\, x) - \frac{1+x}{\pi} & \text{if}\, x < 0 \\ \frac{1}{\pi^2} \sin(\pi\, x) + \frac{1-x}{\pi} & \text{if}\, x \geq 0 \end{cases} \tag{62}$$

$$\sigma^{\mathrm{ex}} = \frac{1}{\pi} \cos(\pi\, x) - \frac{1}{\pi} \tag{63}$$

The absence of tractions at the crack eliminates $\int_\Omega 2\delta_\ell\, \mathbf{N}_{\tilde{u}}^{\mathrm{T}}\, \mathbf{R}^{\mathrm{T}}\, \mathbf{t}_{\mathrm{d}}^{\mathrm{loc}}\, \mathrm{d}\Omega$ and $\int_\Omega 4\delta_\ell\, \mathbf{N}_{\tilde{u}}^{\mathrm{T}}\, \mathbf{R}^{\mathrm{T}}\, \partial \mathbf{t}_{\mathrm{d}}^{\mathrm{loc}} / \partial [\![\mathbf{u}]\!]\, \mathbf{R}\, \mathbf{N}_{\tilde{u}}\, \mathrm{d}\Omega$ in Equations (54)b and (56)c, respectively, enabling direct investigation on the effect of δ_ℓ on the regularised Heaviside function $\mathscr{H}_\ell$, and the associated shifting technique.

6.1.1. Enrichment scheme assessment

We first explore a potential relationship between the phase-field variable d and the enrichment of individual control points, with the objective to find a prescription for the enrichment scheme. Quadratic NURBS is assumed for the discretisation of 25 uniform elements, and phase-field is evaluated analytically through direct evaluation of the exponential decay in Equation (15). Figure 10 shows the displacement (u) and the stress (σ) results, which are compared with the exact analytical solution for three different enrichment criteria and length-scales.

First we explore the non-shifted displacement field $u_\ell^{\mathrm{h}}(\mathbf{x})$, in Equation (59), and compare the results of the enrichment criterion $\mathbf{d} \geq 1\mathrm{e}-1$ shown in Figure 10A. The length-scale $\ell = h/4$ gives the best agreement with respect to the exact solution, even though negligible oscillations are observed for the stress curve at the peak. In comparison with the enrichment scheme in XIGA [73, 74], control points corresponding to the cracked element are enriched, only $\ell = h/4$ matches, while $\ell = 2h/15$ and $\ell = h/20$ are under-enriched. A similar pattern is also observed for $\mathbf{d} \geq 1\mathrm{e}-4$, where $\ell = 2h/15$ coincides with the XIGA enrichment. It is interesting to see the effect of over-enrichment in $\ell = h/4$, where displacement agreement is satisfactory, but oscillations result in stress estimates. $\ell = h/20$ shows under-enrichment, leading to an incorrect displacement jump at the crack. For $\mathbf{d} \geq 1\mathrm{e}-7$, XIGA's enrichment with $\ell = h/20$ returns satisfactory results for both displacement and stress comparisons. For other length-scales, however, over-enrichment exhibit oscillations which are more pronounced for $\ell = h/4$ and less noticeable for $\ell = 2h/15$ (with only one additional column of control points enriched at each side of the crack).

Instability is an immediate consequence of over-enrichment for $u_\ell^{\mathrm{h,\,SH\,(i)}}(\mathbf{x})$ in Figure 10B, as the stiffness matrix becomes singular. This is reminiscent of the ill-conditioning issue of the discrete fracture analysis with over-enrichment. While the combination of under-enrichment and XIGA's recipe renders stable solutions, the errors are significant. Thus, no further investigation is carried out on $u_\ell^{\mathrm{h,\,SH\,(i)}}(\mathbf{x})$. On the other hand, $u_\ell^{\mathrm{h,\,SH\,(ii)}}(\mathbf{x})$ renders stable results for all enrichment scenarios. Again, the best agreement is observed for XIGA's prescription, while, in general, the results are very similar to those of $u_\ell^{\mathrm{h}}(\mathbf{x})$, though with a completely different set of shape functions utilised, see Figure 6.

Overall, the XIGA enrichment recipe appears to be the most suitable op-

tion, irrespective of the phase-field value. According to XIGA, control points corresponding to the cracked element should be enriched. Hereafter, we only investigate the enrichment scheme proposed by XIGA. Another observation is that, by adopting the XIGA's enrichment scheme, stress oscillations slightly appear for $\ell = h/4$, and disappear with smaller length-scales adopted. It can be deduced that, maintaining the XIGA's prescription, the length-scale parameter ℓ should be smaller than $h/4$ in a uniform mesh of length h. The physical interpretation of this choice is that the regularised phase-field variable d_ℓ majorly occupies the cracked element and vanished elsewhere, see Figure 2B. This is in line with the philosophy of extended finite element analysis, which localises the (discontinuous) enriched field within the cracked element.

6.1.2. $\mathbb{p}$-refinement: continuity-order assessment

One of the main features of IGA is the higher inter-element continuity provided by NURBS basis functions, which increases with $\mathbb{p}$-refinement by elevating the continuity-degree of NURBS. A uniform discretisation of 25 elements is adopted following the enrichment scheme prescribed by XIGA. Analytical δ_ℓ defined in Equation (15) is utilised here. The results are presented for displacement and stress estimates, which are compared with the analytical solution, in Figure 11. Two scenarios are explored for displacement field candidates: the non-shifted displacement field $u_\ell^{\mathrm{h}}(\mathbf{x})$ and the shifted $u_\ell^{\mathrm{h,\,SH\,(ii)}}(\mathbf{x})$ format.

Similar to the results in Section 6.1.1, no difference between the results of the non-shifted formula $u_\ell^{\mathrm{h}}(\mathbf{x})$ and the shifted version $u_\ell^{\mathrm{h,\,SH\,(ii)}}(\mathbf{x})$ is observed. Stress oscillations observed for $\ell = h/4$, which are more pronounced for quartic and less for quadratic and cubic NURBS basis functions, while satisfactory results are obtained for other length-scales. This is reminiscent of the conclusion made in the previous section about confining d_ℓ by choosing $\ell < h/4$. Moreover, the good agreement observed in Figure 10 for $\mathbb{p}$-refinement is another validation of the hypothesis about the best enrichment scheme. Therefore, the term "enrichment" refers to the XIGA's recipe in the remainder.

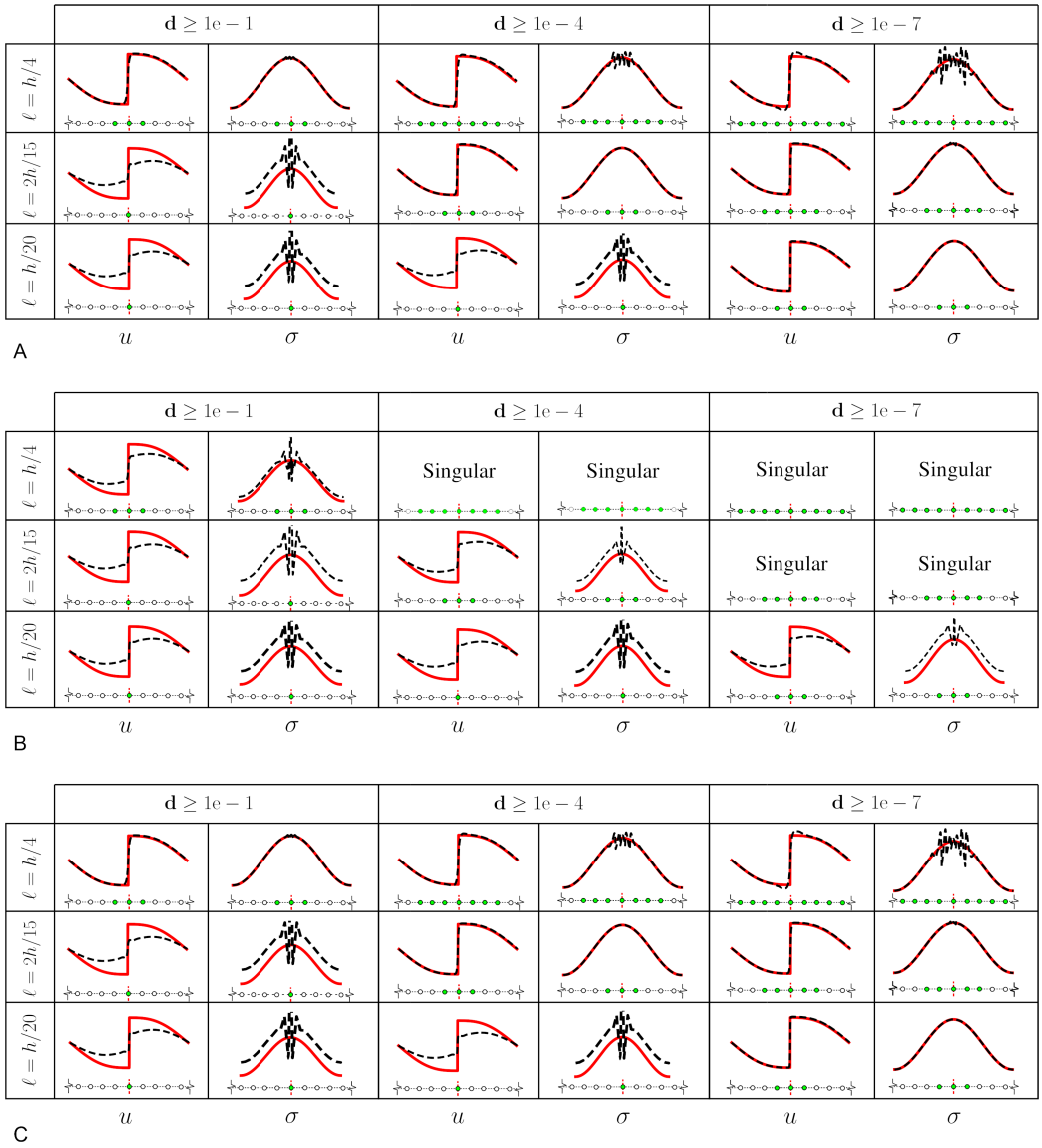

Figure 10: Establishing a relationship between the enriched field and the phase-field variable d for (A) $u_\ell^{\mathrm{h}}(\mathbf{x})$, (B) $u_\ell^{\mathrm{h,\,SH\,(i)}}(\mathbf{x})$ and (C) $u_\ell^{\mathrm{h,\,SH\,(ii)}}(\mathbf{x})$. u and σ denote the displacement and the stress results of our proposed approach, indicated by the dashed black line, compared with the analytical solution, given by the solid red line. Enriched control points corresponding to the enrichment criterion defined on the phase-field variable d are illustrated by green circles. Note that the crack is located at the middle of the plate.

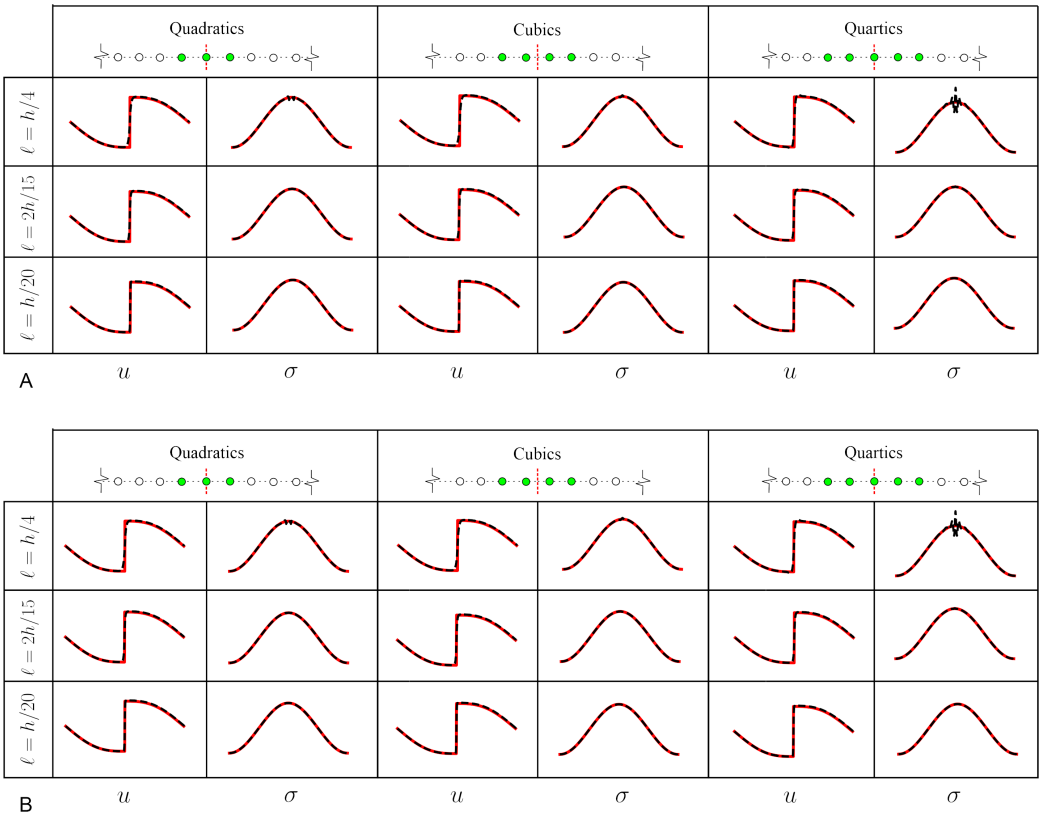

Figure 11: $\mathbb{p}$-refinement comparison for (A) $u_\ell^{\mathrm{h}}(\mathbf{x})$ and (B) $u_\ell^{\mathrm{h,\,SH\,(ii)}}(\mathbf{x})$. Green circles indicate the enriched control points associated with each NURBS. The results are compared with the analytical solution denoted by the red solid curves, comprised of displacement u and stress σ estimates.

6.1.3. Analytical vs numerical phase-field

So far the analytical δ_ℓ in Equation 15 has been utilised in the previous examples. Now, we explore the numerical evaluation of the phase-field formula given in Sections 3.2 and 4.2. A 25-element discretisation with the length scale $\ell = 2h/15$ and the penalty factor $c_0 = 9$ are adopted based on the investigations carried out in Section 4.2. The displacement and stress results are shown in Figure 12 for various combinations of NURBS utilised for mechanical and phase-field problems. A chamfered response is observed for the displacements at a short distance at each side of the crack (see the zoom sections of u in 12A). No substantial difference between analytical and numerical phase-field solutions is observed for the displacements in Figure 12A, with all

solutions showing acceptable accuracy. This is further supported by the L^2 norm error on displacements in Figure 12C, where no significant disparity is observed between the analytical and numerical results. On the other hand, the stresses exhibit different responses for the $\mathbb{p}$-refinement within the mechanical problem, as shown in Figure 12A (see σ columns of Lin (u), Quad (u) and Cub (u)). Unsurprisingly, regardless of phase-field, oscillatory stresses result for linear NURBS utilised in the mechanical problem, as a quadratic approximate is needed to ensure continuous gradient of displacement.

It is best to compare phase-field independently by checking the Γ-error introduced previously, which allows for assessing the quality of δ_ℓ estimates for $\mathbb{p}$-refinement. Figure 12B compare the approximated regularised Dirac-δs against the exact values given by the exponential decay in Equation (15). A tortuous solution is observed for the linear order while quadratic and cubic NURBS guarantee a smooth response. The Γ-error in 12B determines the best NURBS order to satisfy the central identity $\int_\Omega \delta_\ell \mathrm{d}\Omega = \Gamma_\mathrm{d}$, with the orders ranked as quadratic, cubic and linear based on the least error.

In a comparison between numerical and analytical solutions of phase-field, those oscillation caused by the former are more pronounced, which are substantially mitigated by $\mathbb{p}$-refinement, consistently improving as we move away from Lin (u) towards Cub (u), which is also confirmed by the H^1 semi-norm error of the mechanical problem given in Figure 12D, where both analytical and numerical solutions improve with $\mathbb{p}$-refinement. To determine the best combination, H^1 semi-norm errors suggest Cub (u)-Quad (d) by looking at the yellow bars, which is in line the Γ error in Figure 12B for numerical phase-field solutions.

6.2. Cohesive fracture: linear traction-separation relationship

Now, cohesive tractions are considered for a uniform tension test of a plate cracked in the middle, as depicted in Figure 13A. The effect of the length-scale on analytical estimates of δ_ℓ is presented in Figure 13B, which are compared with the numerical estimates in C. The importance of such example lies in the cohesive terms which rely on the quality of the δ_ℓ estimate, particularly in $\mathbf{f}^{\mathrm{int}}_{\tilde{u}}$ and $\mathbf{K}^{\mathrm{int}}_{\tilde{u}\tilde{u}}$ of Equations (54)b and (56)c. A linear traction-separation relationship is utilised, *i.e.*,

$$\mathcal{G}_\mathrm{f} = \frac{1}{2} k \, [\![u_\mathrm{n}]\!]^2, \;\; t_d = k \, [\![u_\mathrm{n}]\!]. \tag{64}$$

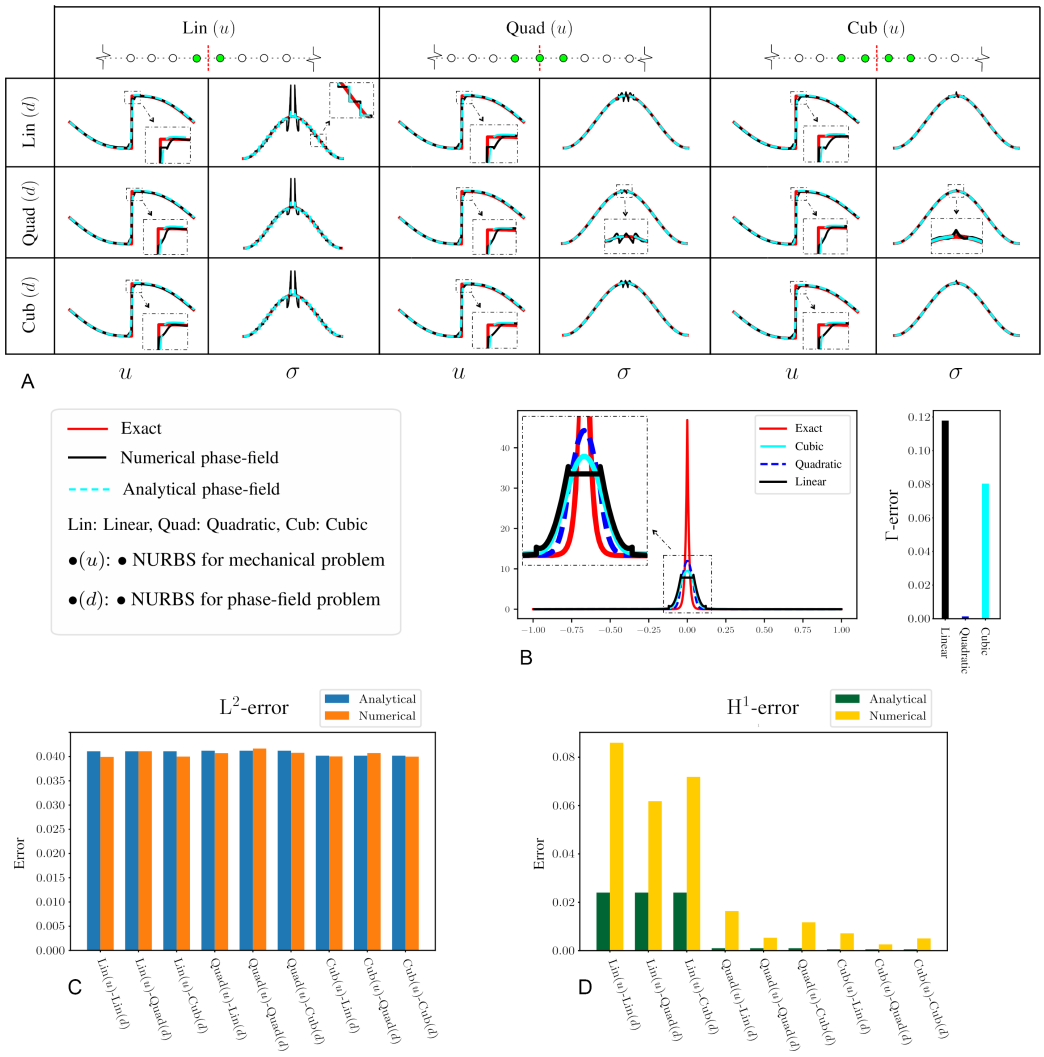

Figure 12: Analytical vs numerical solution for the phase-field problem. Displacement (u) and stress (σ) responses are represented in A for different combinations of NURBS chosen for phase-field and mechanical problems, while B compares numerical δ_ℓ against the analytical (exact) evaluation, assessed by the Γ-error. L^2 norm and H^1 semi-norm errors of the mechanical problem are given in C and D in the form of bar graphs.

with a constant tangent $k = 1$. The material parameters read: Young's modulus $E = 1$; Poisson's ratio $\nu = 0$; and the cross-section area $A = 1$. Due to the symmetry with respect to the $\mathcal{X}$-axis, only 1 element is considered in the $\mathcal{Y}$-direction, reminiscent of a one-dimensional example. The exact solution is given by

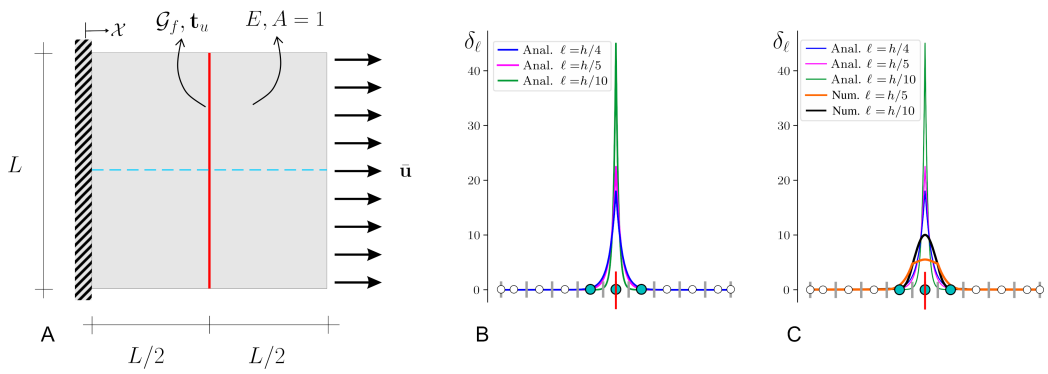

Figure 13: Uniform opening test of (A) a plate cracked at the middle, indicated by the red solid line. Cohesive tractions are characterised by the fracture energy $\mathcal{G}_\mathrm{f}$ and tensile strength t_u at the crack location. δ_ℓ values are plotted for a uniform 9-element discretisation at the dashed blue line. Analytical δ_ℓ values are shown in B, and numerical δ_ℓs are compared to the analytical results in C.

$$u^{\mathrm{ex}} = \begin{cases} \frac{\bar{u}kx}{kL+E} & \text{if } 0 \leq x < L/2 \\ \\ \frac{\bar{u}kx}{kL+E} + \frac{\bar{u}E}{kL+E} & \text{if } L/2 < x \leq L \end{cases} \tag{65}$$

$$\sigma^{\mathrm{ex}} = \frac{\bar{u}kE}{kL+E} \tag{66}$$

where u^{ex} and σ^{ex} indicate the exact displacement and stress, respectively.

Following the results by Section 6.1, two scenarios are considered here: the non-shifted Heaviside function $\mathscr{H}_\ell(x_\mathrm{n})$; the shifted Heaviside function $\mathscr{H}_\ell^{\mathrm{SH\,(ii)}}(x_\mathrm{n})$. The former is already presented in Section 4.3, whose formulations are also valid for the shifted Heaviside by changing $\bullet^{\mathrm{enr}} \leftarrow \bullet^{\mathrm{enr\,(ii)}}$ (see Appendix Appendix A for the definition of these enriched terms).

6.2.1. Length-scale sensitivity analysis

First, we conduct a parametric study of the effect of the length-scale on the mechanical response in the presence of cohesive terms by adopting $\ell \in \{h, h/2, h/4, h/5, h/6, 2h/15, h/8, h/10, h/15, h/20\}$. The results are presented for 9 elements in the top two rows of Figure 14. As observed in Figure 2B, the tangent of analytical d_ℓ at the peak spans the distance 4ℓ, for which we endeavor to find a physical interpretation with respect to the discrete

fracture model. The results in 14A , B, E and F show the optimum solution when 4ℓ is within the cracked element. Specifically, in a uniform mesh of length h ($h = L/9$ in the $\mathcal{X}$-direction), choosing $h = 4\ell$ renders the optimum solution for the non-shifted Heaviside formulation, as shown in Figure 14A and B. A slightly larger element length, $h = 5\ell$ in $\mathcal{X}$-direction, or equivalently a slightly smaller length-scale $\ell = h/5$, exhibits the optimum solution for the shifted Heaviside formulation, $\mathscr{H}_\ell^{\mathrm{SH\,(ii)}}$, depicted in 14E and F. This is in agreement with the findings in Section 6.1. In the case of numerical phase-field presented in Figure 14C, D, G and H, comprehensively studied in Section 6.1, cubic and quadratic NURBS are adopted for the mechanical and phase-field problems, for which $\ell = h/10$ exhibits the optimum solution for the non-shifted and shifted Heaviside formulations.

The length-scale sensitivity analysis provides a physical interpretation that a majority of d_ℓ should be limited to the cracked element, at least the distance occupied by the gradient of d_ℓ at the peak (4ℓ) in Figure 2B, if not entirely. Therefore, $\ell = h/4$ can be used as a reference value for the phase-field regularised PUM, which can vary according to the quality of δ_ℓ estimates. The disparity between the optimum length-scales found for analytical ($\ell \approx h/4$) and numerical ($\ell \ll h/4$) simulations could be attributed to the blunted peak of the numerical estimates, which leads to a wider tangent (lower gradient values) of d_ℓ at the peak (where crack locates), and consequently a flatter δ_ℓ, see Figure 13C for a comparison between analytical and numerical estimates of δ_ℓ.

6.2.2. $\mathbb{h}$*-refinement: discretisation stability*

Next, we investigate the effect of the mesh refinement for analytical and numerical phase-field solutions by choosing the discretisation from the list $\{7, 9, 11, 25, 57, 103\}$ in the $\mathcal{X}$-direction. The results are reported for the optimum length-scales obtained in the previous section, see the bottom two rows in Figure 14. The displacement results, Figures 14I, K, M, O, are difficult to distinguish from the exact solution, while the stress results shown in Figures 14J, L, N and P exhibit clear superiority of the shifted Heaviside formulation, $\mathscr{H}_\ell^{\mathrm{SH\,(ii)}}$. Unsurprisingly, the analytical phase-field formulation (Figures 14J and N) outperforms the numerical implementation (Figures 14L and P) in terms of accuracy. Regarding the stability, all the cases of discretisations converge to the expected results with the trend of better accuracy yielded for finer meshes, as shown by the arrows in Figures 14I, K, M and O. For the displacements, the finest mesh (103 elements) leads to the best results for

both analytical and numerical phase-field solutions. Regarding the stresses, however, the amplitude of the oscillations increases with mesh refinement, but they are also more concentrated to the crack location, see Figures 14J, L, N and P. Between analytical solutions in Figures 14N and J, the stress oscillations for the shifted Heaviside are negligible in value compared with the non-shifted formulation.

The optimum length-scale results from the analytical and numerical studies are collected in Figure 15. As also supported by L^2 norm and H^1 semi-norm errors in E and F, the shifted Heaviside formulation exhibits better accuracy for both displacements and stresses in A and B, respectively. For the numerical phase-field, however, while L^2 norm errors are very close for quadratic and cubic NURBS, the results by the quadratic discretisation excels from the cubic in terms of the H^1 semi-norm errors in H and the stresses reported in D. Even though lower H^1 sermi-norm error is observed for the non-shifted Heaviside function, a more consistent behaviour is observed for the quadratic shifted Heaviside in H. The best results are obtained with the shifted Heaviside function regularised by the analytical phase-field solution, while higher errors and relatively high-amplitude oscillations are observed for non-shifted Heaviside formulation and the stress results of the numerical phase-field solution. Hence, only the shifted Heaviside formulation regularised by analytical phase-field is utilised hereafter.

6.2.3. Sensitivity analysis of singularity

Many approaches have been exploited to mitigate the conditioning issue of the stiffness matrix in extended finite element analysis, as explored in Introduction section. This issue is majorly adhered to two scenarios in which the same reason of inadequate integration of the Heaviside enrichment at one side of the crack can cause the singularity of the stiffness matrix. These scenarios happen when highly disproportionate sections are faced within an element: either the crack path and the element edge align too close to each other; or the crack divides an element too close to a corner. Herein, we explore the hypothesis whether the diffused crack definition can mitigate the ill-conditioning issues. This is motivated by the fact that, unlike discrete fracture models, diffusing the crack leads to a continuous Heaviside function, as explored in Section 2.1. Therefore, within the cracked element, less dependency to proper integration of the Heaviside function is anticipated, since a transition zone for the discontinuity is defined after crack diffusion.

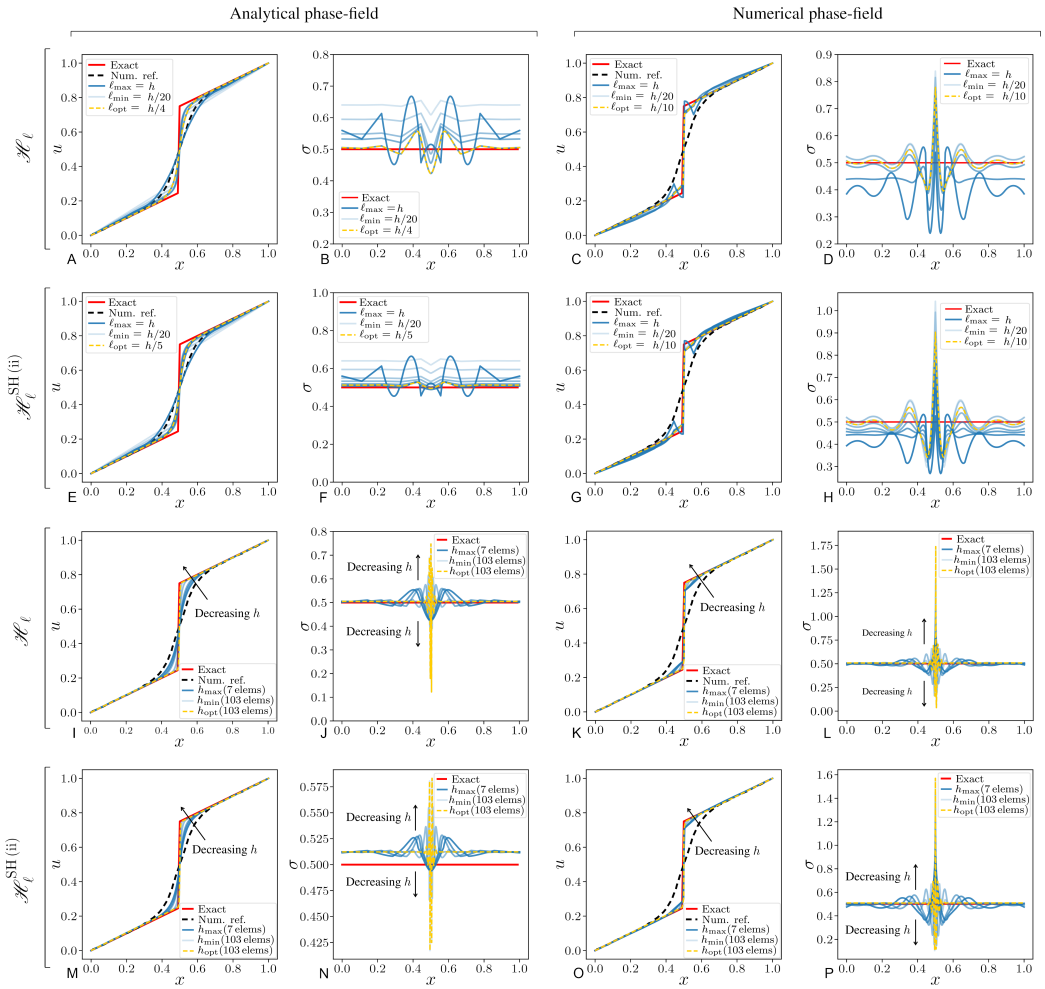

Figure 14: Comparison between the non-shifted ($\mathscr{H}_\ell$) and the shifted ($\mathscr{H}_\ell^{\mathrm{SH\,(ii)}}$) Heaviside formulation of the displacement (u) and stress (σ) results cast for the constant cohesive traction-separation relationship. The results are compared against the exact solution and the numerical result by Verhoosel and de Borst [39], indicated by the solid red and the dashed black lines, respectively. The analytical solution of the phase-field is assumed for the left two columns, while numerical phase-field approach is utilised for the right two columns. Horizontally, the top two rows represent the effect of the length-scale ℓ for the fixed 9×1 elements, whereas mesh refinement is the focus at the bottom two rows.

We have conducted a comprehensive study on the first scenario when the crack aligns with the edge of element at a very close distance. The shifted Heaviside formulation and the analytical phase-field description are adopted for this example with $\ell = \tilde{h}_{\min}/5$, where $\tilde{h}_{\min}$ denotes the min-

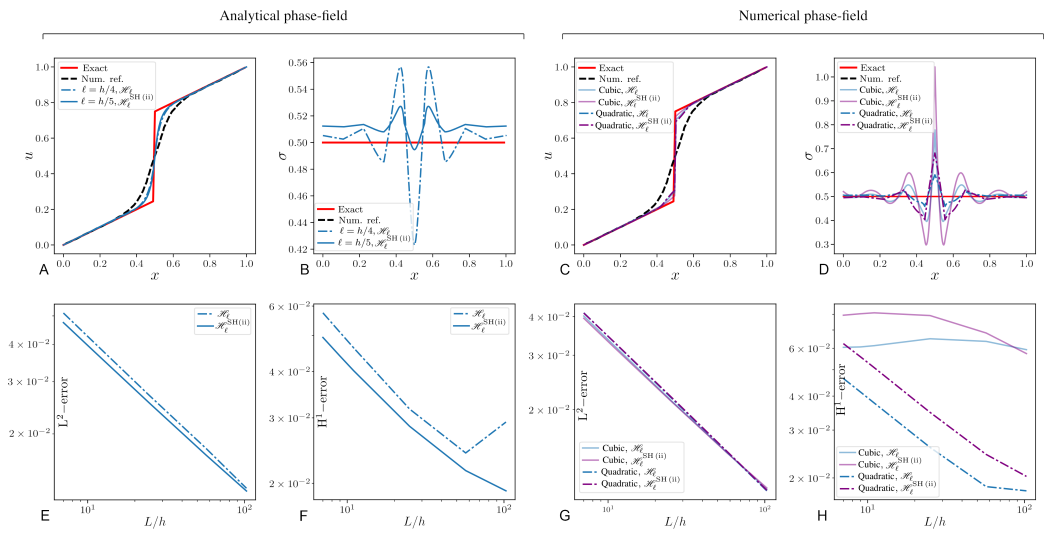

Figure 15: Displacement and stress results of analytical (A and B) and numerical phase-field (C and D) cast for the optimum length-scales specific to the shifted and non-shifted Heaviside functions. 9 elements are considered in the $\mathcal{X}$-direction. L^2 norm and H^1 semi-norm errors are presented in E and F for the analytical phase-field, while G and H show these error norms associated with cubic and quadratic NURBS used for numerical phase-field. Quadratic displacement field is preserved for all cases.

imum length of the enriched elements. The results are shown in Figure 16. To examine the sensitivity of the distance between the element edge (see the blue edge in A) and the crack path to cause singularity, condition numbers of the stiffness matrix are reported for different distances, *i.e.*, $\mathcal{D}_{\text{singularity}} \in \{0.001, 0.002, 0.005, 0.01, 0.05, 0.07143\}$. The results are shown in B comparing the current study with linear interpolation for XFEM and quadratic NURBS for XIGA. For the normalised distances less than 0.005, both XFEM and XIGA report super high condition numbers, while XFEM exhibits the best performance (the least condition number). The results of the current study yields the most stable condition numbers that is approximately equal to XIGA for $\mathcal{D}_{\text{singularity}}/L = 0.071$ at the beginning.

While assessing the condition number of the stiffness matrix is the best indicator of singularity, it is never an assessment of the performance of the mechanical problem. Therefore, we present the displacement and stress results compared with the exact solution and a numerical reference in Figures 16C and D. While displacements return accepted results, the stress plot of the farthest distance are in good agreement with the exact solution. For

$\mathcal{D}_{\text{singularity}}/L = 0.001$, however, the stress plot is slightly worse than the case 0.071. Noteworthy is the fact that the quality of the coarse mesh (7 elements in the $\mathcal{X}$-direction) also plays a significant role in worse stress results, see Figure 16B for a comparison between the two meshes. The accuracy is further assessed by L^2 norm and H^1 semi-norm errors presented in E, where approximately 4×10^{-2} results for both errors at $\mathcal{D}_{\text{singularity}}/L = 1 \times 10^{-11}$. From the stability point of view, the condition number remains in the range $]1.4 \times 10^4 \;\; 1.7 \times 10^4[$ even for $\mathcal{D}_{\text{singularity}}/L = 1 \times 10^{-16}$.

The second scenario of conditioning issue, when the crack divides the element too close to a corner, happens frequently in extended finite element analysis since the crack path and the underlying mesh layout are independent, see the yellow elements in Figure 17B. The results in D and E indicated by the green dashed line exhibit excellent agreement with the exact solution for quadratic NURBS, even though the crack exactly passes the corner of the two yellow elements at the middle of the plate. Noteworthy is the fact that the absence of Kronecker-δ in $\mathcal{C}^{\mathbb{p}-1}$, $\mathbb{p} \geq 2$ has no effect on the ill-conditioning issue, as observed for $\mathcal{C}^1$ in quadratic NURBS.

6.2.4. Irregular discretisation

One of the main features of the phase-field-regularised PUM developed here is the capability of handling irregular discretisations even for the coarsest meshes typically used in discrete fracture models. We have adopted the shifted regularised Heaviside formulation and the analytical phase-field description here, while $\ell = \tilde{h}_{\text{min}}/5$ is the length-scale defined on the minimum element length of the enriched elements. The first case explores moving the edge of the cracked element onto the crack path, see the mesh in Figure 16B for $\mathcal{D}_{\text{singularity}}/L = 0.001$. The results are presented by the dotted blue line in Figures 16C and D, showing excellent agreement for the displacement and accepted result for the stress against exact results. It is noteworthy that the results of the stress could be highly improved with the mesh refinement, as is explored for the next example.

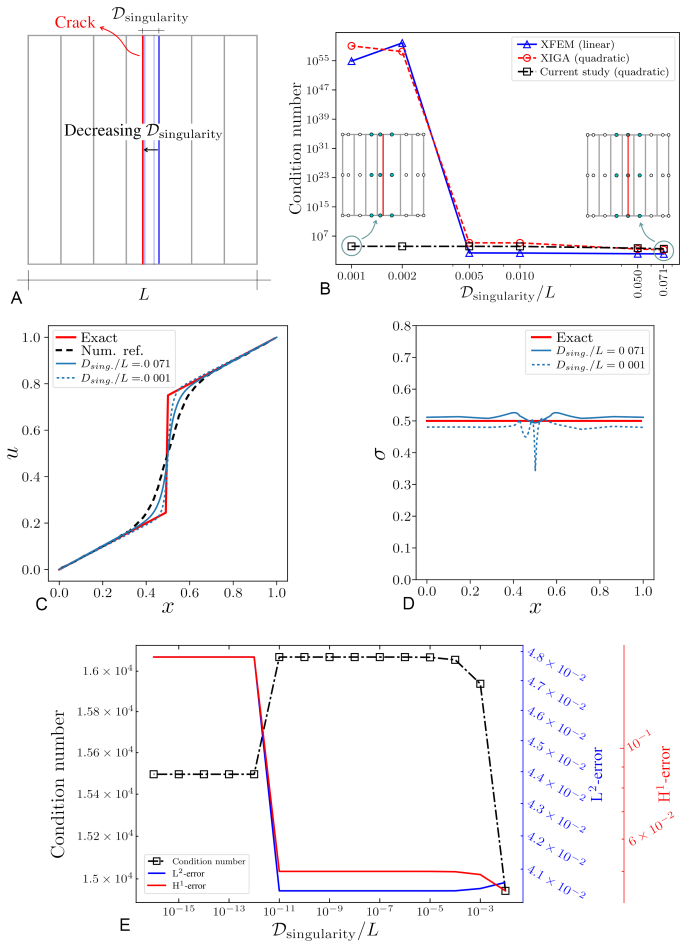

Figure 16: Sensitivity analysis of singularity due to Heaviside enrichment. The blue edge in A gradually approaches the crack and the corresponding condition numbers are plotted for different distances, $\mathcal{D}_{\text{singularity}}$, in B. The results are also compared with XFEM and XIGA. The farthest and closest distances, whose meshes are shown in Figure B, are compared with the exact solution and the numerical reference[39] for the displacement and stress graphs in C and D. L^2 norm and H^1 semi-norm errors are plotted along with their corresponding condition numbers of the current approach in E, in the distance range $\left[1 \times 10^{-16} \quad 1 \times 10^{-2}\right]$.

An inclined mesh is adopted in Figure 17 for the quadratic NURBS (see A and B) to investigate a more complex discretisation example complemented by defining a $\mathcal{C}^0$-continuous line (see the blue line in A and B) by knot insertion [71], while a linear NURBS is also assessed in C. This example provides an additional validation of the enrichment scheme suggested in Section 6.1.1:

control points corresponding to cracked elements are enriched, regardless of the distance to the crack path, which is the only factor in the phase-field variable determination.

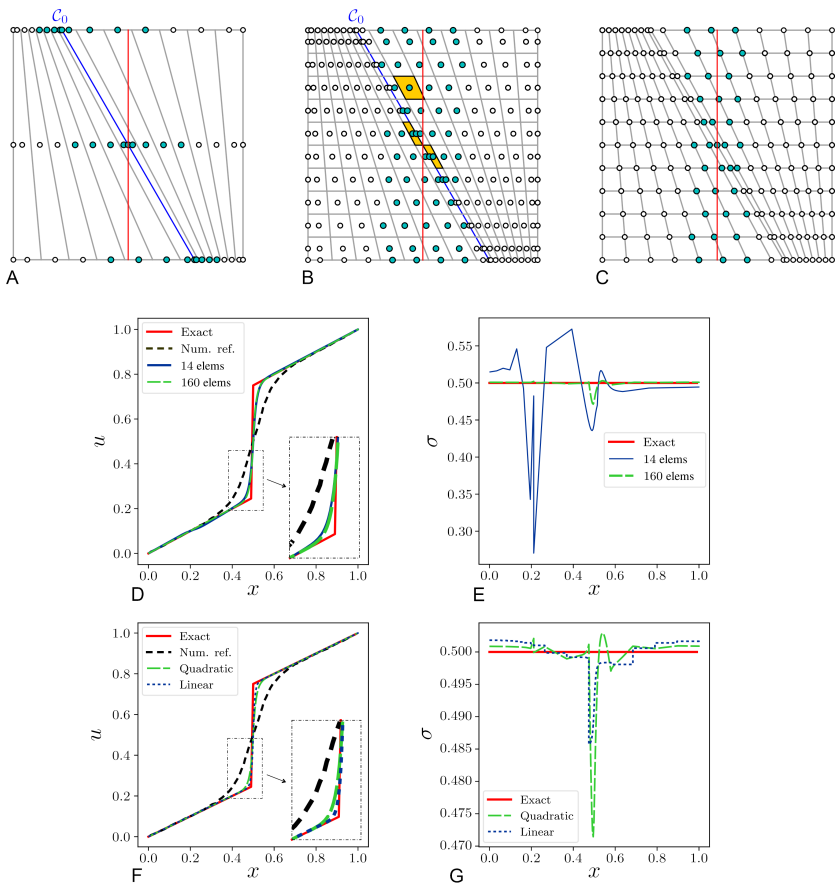

Figure 17: Assessment of phase-field-regularised PUM for irregular meshes shown for (A) 14×1 quadratic, (B) 16×10 quadratic and 16×10 linear NURBS elements. The $\mathcal{C}^0$-continuous line (see the blue line in A and B) is introduced by means of knot insertion to include all typical features of a general mesh in IGA, while all grids of C are $\mathcal{C}^0$-continuous due to linear NURBS adopted. The displacement (D) and stress (E) results are compared for mesh refinement of quadratic NURBS shown in A and B. Utilising the same discretisation, 16×10 elements in F (displacement) and G (stress), the effect of NURBS order is assessed for linear (C) and quadratic (B) NURBS. It is noted that the results are plotted for the top edge of the rectangle.

For quadratic NURBS, the results for the displacement in D are almost identical for the meshes proposed in A and B, while there is an obvious

difference in the stresses shown in E. As observed in A, use of only 1 element in the $\mathcal{Y}$-direction causes a non-uniform enrichment spread over the entire geometry, which is against the localised nature of enrichment. The effect of mesh refinement in B is twofold: a more uniform mesh is introduced for the proposed inclined discretisation; a locally distributed enrichment results due to the smaller support of the refined enriched elements. The stress results significantly improve for the mesh refinement presented in B. In comparison with linear NURBS, however, both displacement and stress results improve when linear NURBS is adopted. Regarding the ill-conditioning of the stiffness matrix, it is proven that the presence or absence of Kronecker-δ has no effect on the performance of our proposed formulation, as both $\mathcal{C}^1$ (quadratic) and $\mathcal{C}^0$ (linear) NURBS have been explored here. Moreover, the satisfactory results of this example refute any relation between the enrichment scheme and the phase-field variable d. It is worth noting that a singular matrix results when the discrete Heaviside formulation, discussed in remark 1 in Section 3, is utilised.

6.2.5. Gauss quadrature sensitivity analysis

So far, as shown previously in Figure 8, the number of Gauss points used for the standard field has been the minimum requirement for full integration $(p+1) \times (q+1)$ using univariate NURBS of orders p and q, while a 9×9 Gauss quadrature has been utilised for the enriched terms to efficiently handle δ_ℓ, a steep exponential decay function. Therefore, we assess whether the quality of the enhanced field $\tilde{u}^{\mathrm{h}}$ is majorly dependent on the quantity of the Gauss points used in the Gauss quadrature. Herein, we examine three irregular meshes, similar to those utilised in Sections 6.2.3 and 6.2.4, in order to find the optimum number of Gauss points needed for integration. The shifted Heaviside formulation given in Equation (61) is only adopted here with $\ell = \tilde{h}_{\min}/5$. We choose a quadratic bivariate NURBS ($p = q = 2$) for the mechanical problem and, therefore, a 3×3 Gauss quadrature is adopted for the standard field. For the phase-field, we exploit the analytical exponential decay to exclude the possible effect of the errors associated with numerical phase-field solutions.

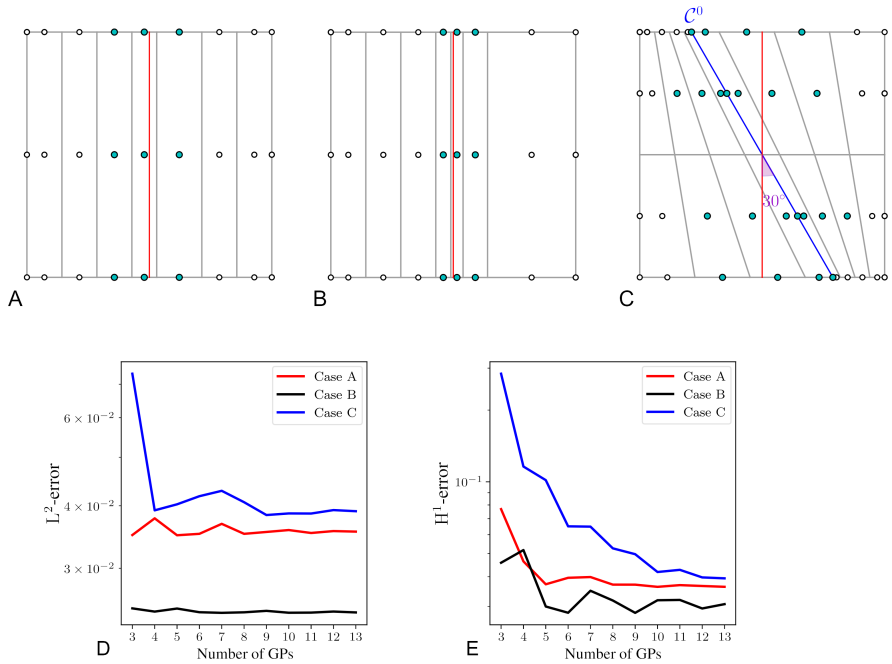

Figure 18: Assessment of the Gauss quadrature for irregular meshes shown for the knot vectors denoted by: $\Xi_x = \{0, 0, 0, 0.1428, 0.2857, 0.4285, 0.53, 0.7142, 0.85714, 1, 1, 1\}$ and $\Xi_y = \{0, 0, 0, 1, 1, 1\}$ in A; $\Xi_x = \{0, 0, 0, 0.1428, 0.2857, 0.4285, 0.49, 0.54, 0.64, 1, 1, 1\}$ and $\Xi_y = \{0, 0, 0, 1, 1, 1\}$ in B; $\Xi_x = \{0, 0, 0, 0.1428, 0.2857, 0.4285, 0.5, 0.5, 0.5714, 0.7142, 0.8571, 1, 1, 1\}$ and $\Xi_y = \{0, 0, 0, 0.5, 1, 1, 1\}$ in C. The L^2 norm and H^1 semi-norm errors are presented in D and E.

The results are presented for L^2 norm and H^1 semi-norm errors of the number of Gauss points in Figure 18. The extent of irregularity increases for the discretisations adopted from A to C. The errors in D and E exhibit uniform results for the meshes in A and B. An inclined mesh is examined in C, while a minimum 2 elements is needed in the $\mathcal{Y}$-direction to prevent the enriched control points from spreading across the entire domain, which can significantly affect the mechanical response, as shown in Section 6.2.4. The results of this case show that a minimum 10 Gauss points are needed to guarantee an almost stable H^1 semi-norm error. The same L^2 norm error exhibits stable errors using a minimum 9 Gauss points used. It is noteworthy that the L^2 norm errors are less restrictive than the H^1 semi-norm errors in terms of the number of Gauss points. In general, it is proved that the number of Gauss points needed are subjective to the quality of discretisation, with

local mesh refinement playing the pivotal role (see Figure 18B).

6.3. Cohesive fracture: nonlinear traction-separation relationship

A nonlinear traction-separation relationship is examined here to better assess the efficacy of the proposed formulation and confirm the conclusions made in previous sections. The geometry and the material properties remain the same as Section 6.2. The energy adopted at the interface reads

$$\mathcal{G}_{\mathrm{f}} = \mathcal{G}_{\mathrm{c}} \left(1 - \left(1 + \frac{[\![u_{\mathrm{n}}]\!]}{v_n} \right) \exp\left(-\frac{[\![u_{\mathrm{n}}]\!]}{v_n} \right) \right) \tag{67}$$

with $v_n = \mathcal{G}_{\mathrm{c}} / \left(t_{\mathrm{u}} \exp(1) \right)$. The traction description at the discontinuity yields

$$t_{\mathrm{d}} = \frac{\partial \mathcal{G}_{\mathrm{f}}}{\partial [\![u_{\mathrm{n}}]\!]} = \mathcal{G}_{\mathrm{c}} \frac{[\![u_{\mathrm{n}}]\!]}{v_n^2} \exp\left(-\frac{[\![u_{\mathrm{n}}]\!]}{v_n} \right) \tag{68}$$

where the critical fracture energy $\mathcal{G}_{\mathrm{c}} = 1$ and the tensile fracture strength $t_{\mathrm{u}} = 0.75$ are adopted for this example. Dealing with a nonlinear problem, an iterative Newton-Raphson solver is adopted with a non-uniform displacement-controlled increments:

$$\bar{\mathbf{u}}^{\mathrm{new}} = \bar{\mathbf{u}}^{\mathrm{old}} + \Delta \bar{\mathbf{u}}, \quad \begin{cases} \Delta \bar{\mathbf{u}} = 0.066667 & \text{if } \bar{\mathbf{u}}^{\mathrm{old}} \leq 2 \\ \Delta \bar{\mathbf{u}} = 0.15 & \text{if } \bar{\mathbf{u}}^{\mathrm{old}} > 2 \end{cases} . \tag{69}$$

Based on the previous sections, the optimum length-scale $\ell = \tilde{h}_{\min}/5$ is adopted here for $\mathscr{H}_{\ell}^{\mathrm{SH\,(ii)}}$. The analytical phase-field, in the form of the exponential decay function, is adopted in this section. The relative energy norm error is calculated by comparing the integral below the force-displacement curve with the energy released by the crack path

$$\text{E-error} = \frac{\left| \int_0^{\infty} f \, \mathrm{d}u - \mathcal{G}_{\mathrm{c}} \cdot l_{\mathrm{cr}} \right|}{\mathcal{G}_{\mathrm{c}} \cdot l_{\mathrm{cr}}} \tag{70}$$

with l_{cr} denoting the crack length.

6.3.1. Irregular discretisation and Gauss points sensitivity analysis

Effect of discretisation irregularity is hardly explored for phase-field models in the presence of nonlinear cohesive relationship. Herein, we have adopted two extreme cases of irregular meshes, see Figures 19A and C, for which the mechanical response is presented through a force-displacement curve plotted for various numbers of Gauss points used for the enriched terms. Based on

the results of the linear traction-opening relation, reported in Section 6.2, a minimum number of 10 Gaussian points return satisfactory results. Hence, we have investigated 10, 11 and 12 points for the Gauss quadrature of enriched term, while maintaining the $(p+1)\times(q+1)$ Gauss quadrature for the standard displacement integration.

The force-displacement curves are shown in Figures 19B and D. While both non-uniform (A) and irregular (C) meshes exhibit satisfactory results for all integration points examined, 12 Gauss points successfully capture the behaviour at the peak, particularly for the inclined mesh in D. The errors are reported in Table 1, showing a clear improvement with 12 GPs for the inclined mesh. Regarding the errors of the non-uniform mesh, the poor quality of discretisation, particularly the significant difference in element sizes, cause considerable error after the peak. This is clearly improved by exploiting a uniform discretisation of the same number of elements examined in Figure 20A, which exhibits good agreement with the exact solution in C.

6.3.2. $\mathbb{h}$*-refinement*

To complement the discretisation stability study in Section 6.2, the effect of discretisation is assessed in the presence of nonlinear traction-separation relationship. This example is pivotal in showcasing the role of PUM in compatibility with coarse meshes. Uniform discretisations (7, 11 and 25 elements) are adopted here, see Figure 20. The mechanical responses in the form of the force-displacement curve are shown in C, which are compared with the exact (discrete) solution and the numerical results by Verhoosel and de Borst [39]. The results are presented for 7 and 25 elements using 12 Gauss points showing excellent agreements with the exact solution, which proves the stability of $\mathbb{h}$-refinement solution using the proposed length-scale. This is supported by the energy norm errors (Equation (70)) reported in Table 1 as well, which quantifies the errors associated with Figure 20C with values less than 1%. In comparison with other numerical techniques, our proposed formulation is compatible with super coarse discretisations, as the results of the 7-element mesh is closer to the exact results than 800 elements utilised by Verhoosel and de Borst [39]. As discussed in details in Remark 2 (see Section 3), the proposed formulation in Verhoosel and de Borst is a special case of the current formulation in the absence of PUM and the consistent displacement jump definition.

Discretisation	Energy norm error	Gauss quadrature		
		10 GPs	11 GPs	12 GPs
Non-unifrom mesh	Relative error (%)	7.7095	8.114	10.482
Inclined mesh	Relative error (%)	4.035	4.090	0.312
Uniform mesh	Relative error (%)	Discretisation		
		7 elems	11 elems	25 elems
		0.826	0.813	0.774

Table 1: Relative energy norm errors for different discretisation cases. Gauss quadrature of the enriched terms is explored by the number of Gauss points (GPs) used for irregular meshes, while mesh refinement is investigated for uniform discretisation.

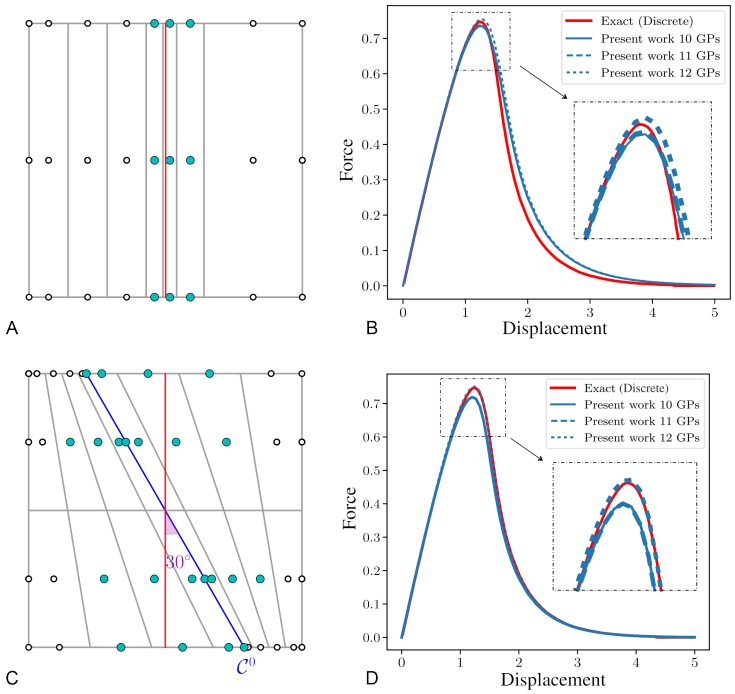

Figure 19: Force-displacement response of irregular discretisation in the presence of cohesive tractions. Two discretisations are investigated: non-uniform mesh $\Xi_x = \{0, 0, 0, 0.14285714, 0.28571429, 0.42857143, 0.49, 0.54, 0.64, 1, 1, 1\}$ and $\Xi_y = \{0, 0, 0, 1, 1, 1\}$ shown in A; inclined mesh $\Xi_x = \{0, 0, 0, 0.14285714, 0.28571429, 0.42857143, 0.5, 0.5, 0.57142857, 0.71428571, 0.85714286, 1, 1, 1\}$ and $\Xi_y = \{0, 0, 0, 0.5, 1, 1, 1\}$ shown in B.

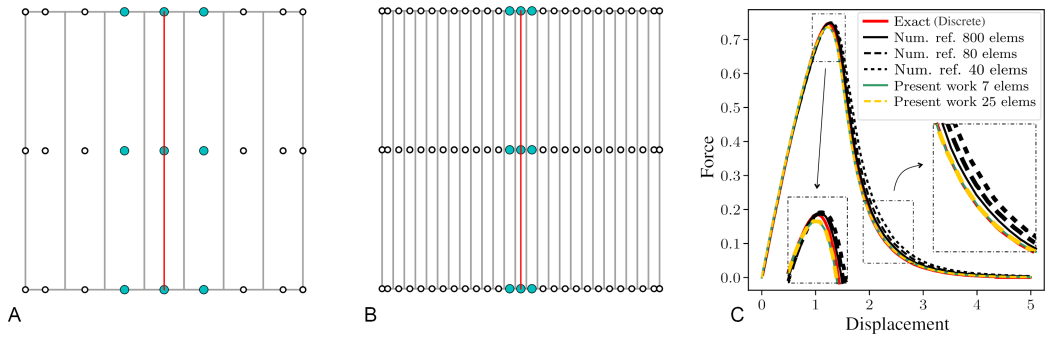

Figure 20: Effect of $\mathbb{h}$-refinement in the presence of non-linear traction-separation relationship. 7 and 25 elements are presented in A and B, while the corresponding force-displacement curves are shown in C, which are compared to those of Verhoosel and de Borst [39] given in black.

6.4. Delamination peel test

Our final example investigates the progressive crack propagation via a peel test, shown in Figure 21, where a traction-free initial slit is considered in a double cantilever beam. The material properties are taken as: the Young's modulus, $E = 100$ MPa; the Poisson's ratio, $\nu = 0.3$; the critical fracture energy, $\mathcal{G}_\mathrm{c} = 0.1$ N/mm; and the tensile fracture strength, $t_\mathrm{u} = 1$ MPa. The traction-crack opening relationship follows the exponential cohesive-zone model, i.e.,

$$\mathcal{G}_\mathrm{f} = -\mathcal{G}_\mathrm{c} \exp\left(-\frac{t_\mathrm{u}}{\mathcal{G}_\mathrm{c}} [\![u_\mathrm{n}]\!]\right), \tag{71}$$

where the cohesive traction relation at the discontinuity yields

$$t_\mathrm{d} = \frac{\partial \mathcal{G}_\mathrm{f}}{\partial [\![u_\mathrm{n}]\!]} = t_\mathrm{u} \exp\left(-\frac{t_\mathrm{u}}{\mathcal{G}_\mathrm{c}} [\![u_\mathrm{n}]\!]\right). \tag{72}$$

A history parameter κ identical to the one discussed in Section 2.2 replaces the displacement opening $[\![u_\mathrm{n}]\!]$ to ensure irreversibility of fracture opening imposed by the Kuhn-Tucker condition.

As shown in Figure 21A, quadratic NURBS elements are used across different spatial discretisations to support mesh objectivity. The enriched control points are highlighted with green circles. A simple enrichment scheme is adopted for crack propagation: all control points belonging to the cracked elements are enriched regardless of the inter-element share of control points,

provided that the enriched terms to be manually removed from the displacement field calculations at all partially-enriched elements in front of the crack tip. The deformed shape after crack propagation is shown in B and C, illustrating displacement and stress fields in the $\mathcal{Y}$-direction, respectively.

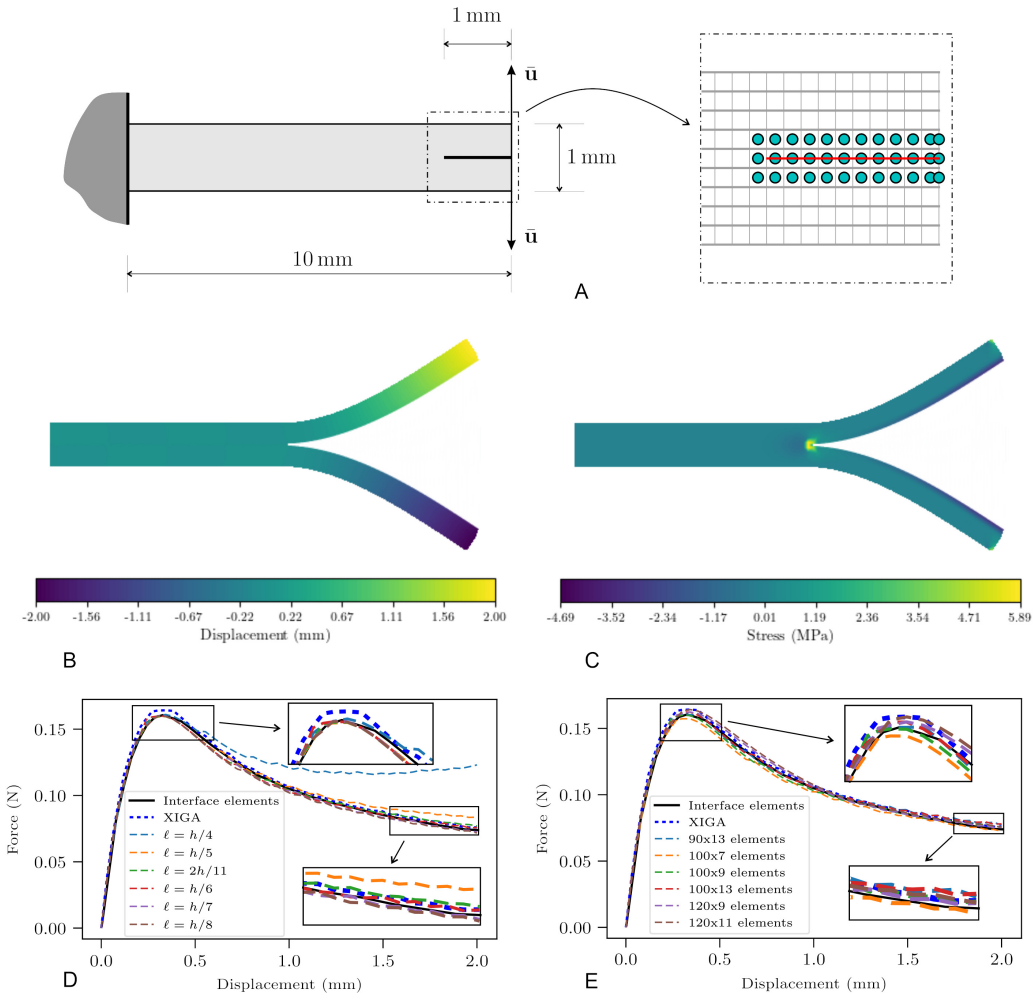

Figure 21: Peel test of (A) a double cantilever beam with an initial slit subjected to prescribed displacement $\bar{\mathbf{u}}$. The zoom box illustrates the enrichment scheme utilised (only enriched control points are shown by green circles). The deformed shape is shown in the forms of the (B) displacement and (C) stress fields in the $\mathcal{Y}$-direction. A parametric study on the internal length scale ℓ is conducted in D, followed by the mesh sensitivity analysis in E. The results are compared with interface elements (90×7) and the XIGA approch (100×9).

So far, we have observed that $\ell = h/5$ is a good choice for stationary crack problems explored in the preceding sections. Nevertheless, we have conducted a parametric study for the progressively propagating crack in the peel test, as investigated in Figure 21D for the fixed mesh 100×9, where the first and the second digits denote the number of elements along the length and the width of the problem, respectively. A converging trend is observed by decreasing the internal length scale ℓ where the factors $\{2/11, 1/6, 1/7, 1/8\}$ render excellent agreement with the results generated by the predefined interface elements and XIGA (see D in Figure 21). This proves that the results are almost insensitive to the length scales below a specific value, a potential alternative to the length scale sensitivity observed in other phase-field contributions.

Next, a mesh sensitivity analysis is presented in Figure 21E, while fixing the internal length scale $\ell = h/6$. The results demonstrate good agreement with those of interface elements and XIGA irrespective of the various spatial discretisations examined with minimal effects on the mechanical response.

It is worth comparing the computational cost of the present study with that of XIGA [74] and the classical phase field model[39]. The comparison is based on the final configuration of the problem, in which the crack propagates for 34 elements after an initial traction-free slit of 10 elements. Rather than reporting computation time — which is subjective to quality of machine's computing processor and would requires rerunning all the comparison candidates with the same machine — we follow the cost estimation approach used in collocation method [88, 87]. Specifically, we correlate the computational cost with the stiffness matrix assembly effort, measured by the number of integration points.

Recalling that the full integration for a bivariate NURBS basis function of order p requires $(p+1) \times (p+1)$, we assume that full integration is employed in [39], even though the exact number of integration points is not reported. Full integration is also used for the standard term in XIGA and our proposed approach. However, the number of points used for the enriched terms differs: XIGA adopts 7×7 integration points, while the current study uses 12×12 integration points for the enriched terms. Additionally, XIGA requires a line integration for the enriched crack interface, for which 9 integration points are used.

Regarding discretisation, we adopt the minimum number of elements reported for this example in [39], namely 50×40 elements, which is comparable to the 100×9 elements used in both XIGA and our proposed approach. XIGA and the current study adopt $\mathcal{C}^1$-continuous discretisations for the standard

and enriched fields. In contrast, the classical phase field model employed $\mathcal{C}^2$-continuous elements for the displacement field, and $\mathcal{C}^0$-continuous elements for both the auxiliary displacement jump and the phase field [39]. It is noted that [39] employed Lagrange polynomials, while the isogeometric version in [41] adopted high-order NURBS with $\mathcal{C}^0$-continuity at element boundaries, which prevents the typical inter-element share of control points. Moreover, the enriched field $\tilde{u}$ in XIGA and in this study is defined locally, forming a narrow band at the vicinity of the crack path. In contrast, the auxiliary displacement jump used in the classical phase field is defined globally. Consequently, the total number of DOFs in the phase field model reaches 40724, while XIGA and our approach use 2520 DOFs. Further details are provided in Table 2.

Type	Computational cost (DOFs & GPs)				Cost reduction
PF	u	v	d	$\sum_{i=u,v,d} \text{cost}_i$	w.r.t PF (%)
	36542 DOFs	2091 DOFs	2091 DOFs	40724 DOFs	—
	32000 GPs	32000 GPs	8000 GPs	72000 GPs	—
PF-PUM	$\hat{u}$	$\tilde{u}$	d	$\sum_{i=\hat{u},\tilde{u},d} \text{cost}_i$	w.r.t PF (%)
	2244 DOFs	276 DOFs	—	2520 DOFs	93.81
	8100 GPs	32400 GPs	—	40500 GPs	43.75
XIGA	$\hat{u}$	$\tilde{u}$	d	$\sum_{i=\hat{u},\tilde{u},d} \text{cost}_i$	w.r.t PF (%)
	2244 DOFs	276 DOFs	—	2520 DOFs	93.81
	8100 GPs	11331 GPs	—	19431 GPs	73.01

Table 2: Computational cost for stiffness matrix assembly, compared across the phase-field (PF) method [39], the proposed phase-field-regularised partition of unity method (PF-PUM), and extended isogeometric analysis (XIGA) [74]. The comparison is based on the number of integration/Gauss points (GPs) and degrees of freedom (DOFs). In this context, u, v, $\hat{u}$, $\tilde{u}$ and d denote the full displacement, the auxiliary displacement jump, the standard displacement, the enriched displacement and phase fields, respectively.

Table 2 presents the computational cost of each approach, specified in terms of DOFs and number of integration/Gauss points, to provide a fair estimation of the stiffness matrix assembly effort. Notably, the current study and XIGA have the same number of DOFs — representing approximately 94% reduction with respect to that of the phase field model. However, the number of Gauss points reveals a higher computational cost for our proposed approach compared to XIGA. While the phase field model requires 72000 integration points, our approach uses 40500, corresponding to a reduction of

approximately 44%. As expected for a discrete approach, the reduction is even more pronounced for XIGA, around 73%. These results demonstrate that, in addition to the other advantages discussed in this study, our proposed approach is significantly more computationally efficient than the classical phase field model. Particularly, in terms of integration points, the proposed approach corresponds to a computational effort that falls between the classical phase field model and XIGA. Moreover, the computational cost of the present study can potentially approach that of XIGA with improved numerical integration for the local exponential decay function in the enriched displacement field.

7. Concluding remarks

A consistent formulation has been constructed for fracture analysis based on the phase-field-regularised Partition of Unity Method (PUM), in which the Dirac-δ in the form of the exponential decay function is approximated for the crack diffusion. The proposed formulation possesses the advantages of a discrete approach, particularly its efficacy with coarse meshes, which is not achieved with conventional phase-field formulations. Adopting PUM allows for an unambiguous displacement jump definition at the discontinuity based on the existing enriched degrees of freedom, leading to an opening behaviour reflecting the true nature of fracture. This also obviates the need to adopt any auxiliary field to compensate the lack of necessary relation between the jump and displacement fields, as utilised in the customary formulation of the cohesive phase-field models.

Enrichment strategy is an inseparable part of PUM for fracture analysis, and has been explored for our proposed formulation for phase-field regularised PUM. After conducting a comprehensive investigation on the potential relationship between the enrichment scheme and the phase-field variable d, it has been proven that the enrichment identical to that of XIGA renders the most satisfactory results, while under-enrichment leads to a wrong displacement jump at the crack, leading to incorrect displacement and stress evaluations. Over-enrichment, on the other hand, leads to acceptable displacement results. However, oscillatory stress estimates are directly proportional to the extent of over-enrichment. For the progressively fracturing cracks, we have adopted the simplest approach by enriching the control points of the cracked elements entirely, regardless of the inter-element share between the intact and cracked elements. However, the enriched terms must be removed from

the formulations when considering the intact elements in front of the crack tip.

In a comparison between the analytical evaluation of the diffused Dirac-δ and the numerical solution of the phase-field problem, quadratic NURBS ($\mathcal{C}^1$-continuous at element boundaries) renders the minimum error for satisfying the identity $\int_\Omega \delta_\ell \, \mathrm{d}\Omega = \Gamma_\mathrm{d}$. For the coupled phase-field and mechanical problems, however, different combinations have been explored. The best solution pertains to cubic NURBS ($\mathcal{C}^2$-continuous at element boundaries) for the mechanical field and quadratic for the phase-field problem. Nevertheless, significant stress oscillations are observed for the phase-field numerical approach in general, while the analytical exponential decay function exhibits satisfactory results, provided that enough Gauss points are utilised for the regularised enriched terms. It has been observed that using 12 Gauss points guarantees proper integration of the discontinuous enriched field, while maintaining the full integration for the intact standard terms ($(p+1) \times (q+1)$ Gauss points for the NURBS surface of orders $p \otimes q$) suffices.

The optimum length-scale has been assessed against $\mathbb{h}$-refinement in the presence of linear and nonlinear traction-separation relationships at the discontinuity. In the examples tested in this article, the minimum length scale to achieve converging results was found to be in the range $h/6 \leq \ell < h/4$. If length scales smaller than the identified thresholds are adopted, the results do not significantly depend on the length scale. When an adequate length scale is adopted, the results are also shown to be insensitive to mesh refinement.

Next, a comprehensive study has been conducted on the conditioning issue associated with extended finite element analysis. Our formulation has successfully resolved the issue by the continuous description of the Heaviside function generated by the diffused representation of the crack. Irregular discretisation has also been investigated for biased mesh layouts to further prove the efficacy of our formulations. Finally, the approach has been benchmarked against crack propagation, indicating excellent agreement with XIGA and interface elements results.

Regarding arbitrary crack paths, our proposed approach offers no improvement over the classical extended finite element analysis, as it borrows the same crack initiation and propagation strategies used in the extended finite element analysis — through the level-set technique, maximum principal stress, and enrichment. By adopting a degradation function, however, the crack initiation and tracking would benefit from automated crack path

monitoring via a phase-field-dependent level-set function. This enhancement will be the focus of our future work.

This work advances the numerical analysis of fracture mechanics, presenting a formulation that delivers robust predictions with relatively low computational costs. Furthermore, it opens up opportunities for future developments and applications. Notably, the current formulation can be extended to accommodate conventional damage-dependent degradation functions, leading to formulations capable of reproducing a wide range of material behaviors and fracture patterns.

Acknowledgments

F. Fathi and G. Torelli gratefully acknowledge the financial support from the European Union (Horizon Europe research and innovation programme, Grant Agreement No 101123293, "SINCERE–The Second Life of Modern Period Architecture: Resilient and Adaptive Renovation towards Net-Zero Carbon Heritage Buildings" project), with UK-specific Horizon Europe Guarantee Extension via UKRI grant 10089449. For the purpose of open access, the author has applied a Creative Commons Attribution (CC BY) licence to any Author Accepted Manuscript version arising.

Appendix A. Enriched shape-function vector and strain-displacement matrix

For simplicity, we define the following notation for the enriched strain-displacement and basis function matrices

$$\mathbf{B}_{u_i}^{\mathrm{enr}} = \mathscr{H}_{\Gamma_{\mathrm{d}}}\left(x_{\mathrm{n}}\right)\left(1-2\ell\delta_{\ell}\right)\mathbf{B}_{u_i} = \mathscr{H}_{\Gamma_{\mathrm{d}}}\left(x_{\mathrm{n}}\right)\left(1-2\ell\delta_{\ell}\right)\begin{bmatrix} \frac{\partial N_{u_i}}{\partial X_1} & 0 \\ 0 & \frac{\partial N_{u_i}}{\partial X_2} \\ \frac{\partial N_{u_i}}{\partial X_2} & \frac{\partial N_{u_i}}{\partial X_1} \end{bmatrix} \quad \forall i \in \mathcal{I}^{\mathrm{enr}} \tag{A.1a}$$

$$\mathbf{N}_{u_i}^{\mathrm{enr}} = \mathscr{H}_{\Gamma_{\mathrm{d}}}\left(x_{\mathrm{n}}\right)\left(1-2\ell\delta_{\ell}\right)\mathbf{N}_{u_i} = \mathscr{H}_{\Gamma_{\mathrm{d}}}\left(x_{\mathrm{n}}\right)\left(1-2\ell\delta_{\ell}\right)\begin{bmatrix} N_{u_i} & 0 \\ 0 & N_{u_i} \end{bmatrix} \quad \forall i \in \mathcal{I}^{\mathrm{enr}} \tag{A.1b}$$

where x_{n} denotes the normal signed distance of the point $\mathbf{x}$ from the crack path. The formulation for the shifted Heaviside function, *i.e.*, $\mathscr{H}_{\ell}^{\mathrm{SH\,(ii)}}$ is given next

$$\mathbf{B}_{u_i}^{\mathrm{enr\,(ii)}} = \left(\mathscr{H}_{\Gamma_{\mathrm{d}}}\left(x_{\mathrm{n}}\right)\left(1-2\ell\,\delta_{\ell}\left(x_{\mathrm{n}}\right)\right) - \mathscr{H}_{\Gamma_{\mathrm{d}}}\left(x_{\mathrm{n}}^{i}\right)\left(1-2\ell\,\delta_{\ell}\left(x_{\mathrm{n}}^{i}\right)\right)\right) \begin{bmatrix} \frac{\partial N_{u_i}}{\partial X_1} & 0 \\ 0 & \frac{\partial N_{u_i}}{\partial X_2} \\ \frac{\partial N_{u_i}}{\partial X_2} & \frac{\partial N_{u_i}}{\partial X_1} \end{bmatrix} \qquad \forall i \in \mathcal{I}^{\mathrm{enr}} \tag{A.2a}$$

$$\mathbf{N}_{u_i}^{\mathrm{enr\,(ii)}} = \left(\mathscr{H}_{\Gamma_{\mathrm{d}}}\left(x_{\mathrm{n}}\right)\left(1-2\ell\,\delta_{\ell}\left(x_{\mathrm{n}}\right)\right) - \mathscr{H}_{\Gamma_{\mathrm{d}}}\left(x_{\mathrm{n}}^{i}\right)\left(1-2\ell\,\delta_{\ell}\left(x_{\mathrm{n}}^{i}\right)\right)\right) \begin{bmatrix} N_{u_i} & 0 \\ 0 & N_{u_i} \end{bmatrix} \qquad \forall i \in \mathcal{I}^{\mathrm{enr}}. \tag{A.2b}$$

References

[1] A. A. Griffith, The phenomena of rupture and flow in solids, Philosophical Transactions of the Royal Society of London 221 (582-593) (1921) 163–198.

[2] C. E. Inglis, Stresses in a plate due to the presence of cracks and sharp corners, Transactions of the Institution of Naval Architects 55 (1913) 219–241.

[3] G. R. Irwin, Analysis of stresses and strains near the end of a crack traversing a plate, Journal of Applied Mechanics 24 (1957) 361–364.

[4] J. R. Rice, A path independent integral and the approximate analysis of strain concentration by notches and cracks, Journal of Applied Mechanics 35 (2) (1968) 379–386.

[5] A. R. Ingraffea, V. Saouma, Numerical Modeling of Discrete Crack Propagation in Reinforced and Plain Concrete, in: Fracture Mechanics of Concrete: Structural Application and Numerical Calculation, Springer, 1985, pp. 171–225.

[6] M. Ortiz, Y. Leroy, A. Needleman, A finite element method for localized failure analysis, Computer Methods in Applied Mechanics and Engineering 61 (2) (1987) 189–214.

[7] T. Belytschko, J. Fish, B. E. Engelmann, A finite element with embedded localization zones, Computer Methods in Applied Mechanics and Engineering 70 (1) (1988) 59–89.

[8] J. C. Simo, J. Oliver, F. Armero, An analysis of strong discontinuities induced by strain-softening in rate-independent inelastic solids, Computational Mechanics 12 (5) (1993) 277–296.

[9] M. Jirásek, Comparative study on finite elements with embedded discontinuities, Computer Methods in Applied Mechanics and Engineering 188 (1-3) (2000) 307–330.

[10] J. Oliver, A. E. Huespe, E. Samaniego, A study on finite elements for capturing strong discontinuities, International Journal for Numerical Methods in Engineering 56 (14) (2003) 2135–2161.

[11] R. de Borst, H.-B. Mühlhaus, Gradient-dependent plasticity: formulation and algorithmic aspects, International Journal for Numerical Methods in Engineering 35 (3) (1992) 521–539.

[12] R. H. Peerlings, R. de Borst, W. Brekelmans, M. G. Geers, Gradient-enhanced damage modelling of concrete fracture, Mechanics of Cohesive-frictional Materials 3 (4) (1998) 323–342.

[13] G. Pijaudier-Cabot, Z. P. Bažant, Nonlocal damage theory, Journal of Engineering Mechanics 113 (10) (1987) 1512–1533.

[14] L. Chen, B. Li, R. de Borst, Integral form of mixed-mode crack opening in the phase field method, Theoretical and Applied Fracture Mechanics 132 (2024) 104481.

[15] L. Chen, B. Li, G. Cui, R. de Borst, A comparison of approaches to compute the crack opening/sliding within the phase-field method, Theoretical and Applied Fracture Mechanics 136 (2025) 104818.

[16] O. Allix, P. Ladevèze, Interlaminar interface modelling for the prediction of delamination, Composite Structures 22 (4) (1992) 235–242.

[17] J. C. Schellekens, R. de Borst, On the numerical integration of interface elements, International Journal for Numerical Methods in Engineering 36 (1) (1993) 43–66.

[18] I. Babuška, J. M. Melenk, The partition of unity method, International Journal for Numerical Methods in Engineering 40 (4) (1997) 727–758.

[19] T. Belytschko, T. Black, Elastic crack growth in finite elements with minimal remeshing, International Journal for Numerical Methods in Engineering 45 (5) (1999) 601–620.

[20] E. De Luycker, D. J. Benson, T. Belytschko, Y. Bazilevs, M. C. Hsu, X-FEM in isogeometric analysis for linear fracture mechanics, International Journal for Numerical Methods in Engineering 87 (2011) 541–565.

[21] D. S. Dugdale, Yielding of steel sheets containing slits, Journal of the Mechanics and Physics of Solids 8 (2) (1960) 100–104.

[22] G. I. Barenblatt, The mathematical theory of equilibrium cracks in brittle fracture, Advances in Applied Mechanics 7 (1962) 55–129.

[23] G. Alfano, M. A. Crisfield, Finite element interface models for the delamination analysis of laminated composites: mechanical and computational issues, International Journal for Numerical Methods in Engineering 50 (7) (2001) 1701–1736.

[24] G. N. Wells, L. J. Sluys, A new method for modelling cohesive cracks using finite elements, International Journal for Numerical Methods in Engineering 50 (12) (2001) 2667–2682.

[25] G. A. Francfort, J.-J. Marigo, Revisiting brittle fracture as an energy minimization problem, Journal of the Mechanics and Physics of Solids 46 (8) (1998) 1319–1342.

[26] B. Bourdin, G. A. Francfort, J.-J. Marigo, Numerical experiments in revisited brittle fracture, Journal of the Mechanics and Physics of Solids 48 (4) (2000) 797–826.

[27] B. Bourdin, G. A. Francfort, J.-J. Marigo, The variational approach to fracture, Journal of Elasticity 91 (2008) 5–148.

[28] H. Amor, J.-J. Marigo, C. Maurini, Regularized formulation of the variational brittle fracture with unilateral contact: Numerical experiments, Journal of the Mechanics and Physics of Solids 57 (8) (2009) 1209–1229.

[29] C. Miehe, F. Welschinger, M. Hofacker, Thermodynamically consistent phase-field models of fracture: Variational principles and multi-field fe implementations, International Journal for Numerical Methods in Engineering 83 (10) (2010) 1273–1311.

[30] C. Miehe, M. Hofacker, F. Welschinger, A phase field model for rate-independent crack propagation: Robust algorithmic implementation based on operator splits, Computer Methods in Applied Mechanics and Engineering 199 (45-48) (2010) 2765–2778.

[31] M. J. Borden, C. V. Verhoosel, M. A. Scott, T. J. Hughes, C. M. Landis, A phase-field description of dynamic brittle fracture, Computer Methods in Applied Mechanics and Engineering 217 (2012) 77–95.

[32] J. Vignollet, S. May, R. de Borst, C. V. Verhoosel, Phase-field models for brittle and cohesive fracture, Meccanica 49 (11) (2014) 2587–2601.

[33] M. Ambati, T. Gerasimov, L. De Lorenzis, A review on phase-field models of brittle fracture and a new fast hybrid formulation, Computational Mechanics 55 (2015) 383–405.

[34] F. P. Duda, A. Ciarbonetti, P. J. Sánchez, A. E. Huespe, A phase-field/gradient damage model for brittle fracture in elastic–plastic solids, International Journal of Plasticity 65 (2015) 269–296.

[35] R. de Borst, C. V. Verhoosel, Gradient damage vs phase-field approaches for fracture: Similarities and differences, Computer Methods in Applied Mechanics and Engineering 312 (2016) 78–94.

[36] M. Ambati, T. Gerasimov, L. De Lorenzis, Phase-field modeling of ductile fracture, Computational Mechanics 55 (2015) 1017–1040.

[37] M. J. Borden, T. J. Hughes, C. M. Landis, A. Anvari, I. J. Lee, A phase-field formulation for fracture in ductile materials: Finite deformation balance law derivation, plastic degradation, and stress triaxiality effects, Computer Methods in Applied Mechanics and Engineering 312 (2016) 130–166.

[38] M. Ambati, R. Kruse, L. De Lorenzis, A phase-field model for ductile fracture at finite strains and its experimental verification, Computational Mechanics 57 (2016) 149–167.

[39] C. V. Verhoosel, R. de Borst, A phase-field model for cohesive fracture, International Journal for Numerical Methods in Engineering 96 (1) (2013) 43–62.

[40] T.-T. Nguyen, J. Yvonnet, Q.-Z. Zhu, M. Bornert, C. Chateau, A phase-field method for computational modeling of interfacial damage interacting with crack propagation in realistic microstructures obtained by microtomography, Computer Methods in Applied Mechanics and Engineering 312 (2016) 567–595.

[41] Y. Ghaffari Motlagh, R. de Borst, Considerations on a phase-field model for adhesive fracture, International Journal for Numerical Methods in Engineering 121 (13) (2020) 2946–2963.

[42] L. Chen, R. de Borst, Phase-field regularised cohesive zone model for interface modelling, Theoretical and Applied Fracture Mechanics 122 (2022) 103630.

[43] R. J. Geelen, Y. Liu, T. Hu, M. R. Tupek, J. E. Dolbow, A phase-field formulation for dynamic cohesive fracture, Computer Methods in Applied Mechanics and Engineering 348 (2019) 680–711.

[44] A. Baktheer, E. Martínez-Pañeda, F. Aldakheel, Phase field cohesive zone modeling for fatigue crack propagation in quasi-brittle materials, Computer Methods in Applied Mechanics and Engineering 422 (2024) 116834.

[45] E. Lorentz, V. Godard, Gradient damage models: toward full-scale computations, Computer Methods in Applied Mechanics and Engineering 200 (21-22) (2011) 1927–1944.

[46] E. Benvenuti, A. Tralli, G. Ventura, A regularized XFEM model for the transition from continuous to discontinuous displacements, International Journal for Numerical Methods in Engineering 74 (6) (2008) 911–944.

[47] S. Osher, J. A. Sethian, Fronts propagating with curvature-dependent speed: Algorithms based on Hamilton-Jacobi formulations, Journal of Computational Physics 79 (1) (1988) 12–49.

[48] M. Stolarska, D. L. Chopp, N. Moës, T. Belytschko, Modelling crack growth by level sets in the extended finite element method, International Journal for Numerical Methods in Engineering 51 (8) (2001) 943–960.

[49] J. A. Sethian, A fast marching level set method for monotonically advancing fronts., Proceedings of the National Academy of Sciences 93 (4) (1996) 1591–1595.

[50] D. Chopp, N. Sukumar, Fatigue crack propagation of multiple coplanar cracks with the coupled extended finite element/fast marching method, International Journal of Engineering Science 41 (8) (2003) 845–869.

[51] H. K. A. Attar, Modeling 3d crack coalescence with the xfem and level sets, Institut für Kontinuumsmechanik, Gottfried Wilhelm Leibniz Universität Hannover, 2019.

[52] R. Geelen, J. Plews, M. Tupek, J. Dolbow, An extended/generalized phase-field finite element method for crack growth with global-local enrichment, International Journal for Numerical Methods in Engineering 121 (11) (2020) 2534–2557.

[53] B. Giovanardi, A. Scotti, L. Formaggia, A hybrid XFEM–phase field (xfield) method for crack propagation in brittle elastic materials, Computer Methods in Applied Mechanics and Engineering 320 (2017) 396–420.

[54] C. Kuhn, R. Müller, A new finite element technique for a phase field model of brittle fracture, Journal of Theoretical and Applied Mechanics 49 (4) (2011) 1115–1133.

[55] S. Loehnert, C. Krüger, V. Klempt, L. Munk, An enriched phase-field method for the efficient simulation of fracture processes, Computational Mechanics 71 (5) (2023) 1015–1039.

[56] N. Moës, C. Stolz, P.-E. Bernard, N. Chevaugeon, A level set based model for damage growth: the thick level set approach, International Journal for Numerical Methods in Engineering 86 (3) (2011) 358–380.

[57] F. Cazes, N. Moës, Comparison of a phase-field model and of a thick level set model for brittle and quasi-brittle fracture, International Journal for Numerical Methods in Engineering 103 (2) (2015) 114–143.

[58] I. Babuška, U. Banerjee, Stable generalized finite element method (sgfem), Computer Methods in Applied Mechanics and Engineering 201 (2012) 91–111.

[59] A. G. Sanchez-Rivadeneira, C. A. Duarte, A stable generalized/extended fem with discontinuous interpolants for fracture mechanics, Computer Methods in Applied Mechanics and Engineering 345 (2019) 876–918.

[60] T. Strouboulis, I. Babuška, K. Copps, The design and analysis of the generalized finite element method, Computer Methods in Applied Mechanics and Engineering 181 (1-3) (2000) 43–69.

[61] T. Strouboulis, K. Copps, I. Babuška, The generalized finite element method, Computer Methods in Applied Mechanics and Engineering 190 (32-33) (2001) 4081–4193.

[62] A. Menk, S. P. Bordas, A robust preconditioning technique for the extended finite element method, International Journal for Numerical Methods in Engineering 85 (13) (2011) 1609–1632.

[63] V. Gupta, C. A. Duarte, I. Babuška, U. Banerjee, A stable and optimally convergent generalized fem (sgfem) for linear elastic fracture mechanics, Computer Methods in Applied Mechanics and Engineering 266 (2013) 23–39.

[64] V. Gupta, C. A. Duarte, I. Babuška, U. Banerjee, Stable gfem (sgfem): Improved conditioning and accuracy of gfem/xfem for three-dimensional fracture mechanics, Computer Methods in Applied Mechanics and Engineering 289 (2015) 355–386.

[65] Q. Zhang, I. Babuška, U. Banerjee, Robustness in stable generalized finite element methods (sgfem) applied to poisson problems with crack singularities, Computer Methods in Applied Mechanics and Engineering 311 (2016) 476–502.

[66] J. Dolbow, N. Moës, T. Belytschko, Discontinuous enrichment in finite elements with a partition of unity method, Finite Elements in Analysis and Design 36 (3-4) (2000) 235–260.

[67] J. J. Remmers, R. de Borst, A. Needleman, The simulation of dynamic crack propagation using the cohesive segments method, Journal of the Mechanics and Physics of Solids 56 (1) (2008) 70–92.

[68] A. Sillem, A. Simone, L. J. Sluys, The orthonormalized generalized finite element method–ogfem: Efficient and stable reduction of approximation errors through multiple orthonormalized enriched basis functions, Computer Methods in Applied Mechanics and Engineering 287 (2015) 112–149.

[69] S. D. Rao, S. Raju, Orthogonalized Generalized Iso-Geometric Analysis (OGIGA) and its applications to problems of fracture mechanics, Computer Methods in Applied Mechanics and Engineering 372 (2020) 113427.

[70] T. J. R. Hughes, J. A. Cottrell, Y. Bazilevs, Isogeometric analysis: CAD, finite elements, NURBS, exact geometry and mesh refinement, Computer Methods in Applied Mechanics and Engineering 194 (39-41) (2005) 4135–4195.

[71] C. V. Verhoosel, M. A. Scott, R. de Borst, T. J. R. Hughes, An isogeometric approach to cohesive zone modeling, International Journal for Numerical Methods in Engineering 87 (2011) 336–360.

[72] J. A. Evans, Y. Bazilevs, I. Babuška, T. J. Hughes, n-widths, sup–infs, and optimality ratios for the k-version of the isogeometric finite element method, Computer Methods in Applied Mechanics and Engineering 198 (21-26) (2009) 1726–1741.

[73] F. Fathi, R. de Borst, Geometrically nonlinear extended isogeometric analysis for cohesive fracture with applications to delamination in composites, Finite Elements in Analysis and Design 191 (2021) 103527.

[74] F. Fathi, L. Chen, R. de Borst, Extended isogeometric analysis for cohesive fracture, International Journal for Numerical Methods in Engineering 121 (20) (2020) 4584–4613.

[75] J. Vignollet, S. May, R. de Borst, On the numerical integration of isogeometric interface elements, International Journal for Numerical Methods in Engineering 102 (11) (2015) 1733–1749.

[76] F. Fathi, L. Chen, R. de Borst, X-IGALME: Isogeometric analysis extended with local maximum entropy for fracture analysis, International Journal for Numerical Methods in Engineering (2021).

[77] B. Patzák, M. Jirásek, Process zone resolution by extended finite elements, Engineering Fracture Mechanics 70 (7-8) (2003) 957–977.

[78] E. Benvenuti, A regularized XFEM framework for embedded cohesive interfaces, Computer Methods in Applied Mechanics and Engineering 197 (49-50) (2008) 4367–4378.

[79] M. J. Borden, M. A. Scott, J. A. Evans, T. J. Hughes, Isogeometric finite element data structures based on bézier extraction of NURBS, International Journal for Numerical Methods in Engineering 87 (1-5) (2011) 15–47.

[80] C. A. Duarte, J. T. Oden, An hp adaptive method using clouds, Computer Methods in Applied Mechanics and Engineering 139 (1-4) (1996) 237–262.

[81] T.-P. Fries, T. Belytschko, The extended/generalized finite element method: an overview of the method and its applications, International Journal for Numerical Methods in Engineering 84 (3) (2010) 253–304.

[82] A. R. Khoei, Extended Finite Element Method: Theory and Applications, John Wiley & Sons, 2014.

[83] S. Mohammadi, Extended Finite Element Method: for Fracture Analysis of Structures, John Wiley & Sons, 2008.

[84] F. Fathi, L. Chen, T. Hageman, R. de Borst, Extended isogeometric analysis of a progressively fracturing fluid-saturated porous medium, International Journal for Numerical Methods in Engineering 123 (8) (2022) 1861–1881.

[85] K. Park, G. H. Paulino, Cohesive zone models: a critical review of traction-separation relationships across fracture surfaces, Applied Mechanics Reviews 64 (6) (2011) 060802.

[86] R. de Borst, L. Chen, Phase-field modelling of cohesive interface failure, International Journal for Numerical Methods in Engineering 125 (9) (2024) e7412.

[87] F. Fathi, J. E. Oakley, R. de Borst, An extended isogeometric collocation method for fracture analysis, International Journal for Numerical Methods in Engineering (2024) e7507.

[88] D. Schillinger, M. J. Borden, H. K. Stolarski, Isogeometric collocation for phase-field fracture models, Computer Methods in Applied Mechanics and Engineering 284 (2015) 583–610.

[89] R. de Borst, M. A. Crisfield, J. J. C. Remmers, C. V. Verhoosel, Nonlinear Finite Element Analysis of Solids and Structures, John Wiley & Sons, 2012.

[90] T. J. R. Hughes, The Finite Element Method: Linear Static and Dynamic Finite Element Analysis, Courier Corporation, 2012.

[91] L. Piegl, W. Tiller, The NURBS Book, Springer Science & Business Media, 1996.

[92] M. Jirásek, Nonlocal damage mechanics, Revue Européenne de Génie Civil 11 (7-8) (2007) 993–1021.